

First-principles calculations of solute transport in zirconium: Vacancy-mediated diffusion with metastable states and interstitial diffusion

Abhinav C. P. Jain,^{1,*} Patrick A. Burr,^{2,3,†} and Dallas R. Trinkle^{1,‡}

¹*Department of Materials Science and Engineering, University of Illinois at Urbana-Champaign, Urbana, Illinois 61801, USA*

²*School of Mechanical and Manufacturing Engineering, The University of New South Wales, New South Wales, 2052, Australia*

³*Materials Department, Imperial College London, London, SW7 2AZ, United Kingdom*



(Received 30 September 2018; revised manuscript received 18 February 2019; published 18 March 2019)

Zirconium alloys are the most widely used nuclear fuel cladding materials for light water power reactors where irradiation damage causes solute redistribution, leading to degradation of alloy properties such as corrosion resistance. Designing radiation-tolerant zirconium alloys requires a thorough understanding of the atomic-scale transport behavior of the alloying elements in Zr. We perform density function theory calculations to investigate the diffusion of Sn, Cr, Fe, Be, Al, and Ni in the hexagonal close-packed (HCP) Zr matrix. We develop a methodology to accurately model the metastable vacancy states along the basal migration path, known to occur in group IV metals. We compute the vacancy-mediated solute diffusion coefficients and drag ratios using the kinetic Monte Carlo method and an analytic Green's function method—the agreement between the two validates our methodology. The computed diffusion coefficients of Sn and Al show good agreement with the experimental data and we expect these solutes to diffuse via the vacancy-mediated mechanism. We use a Green's function approach, parameterized with data from density functional theory calculations, to compute the interstitial diffusion coefficients of Cr, Fe, Be, and Ni in the HCP Zr lattice. The computed diffusion coefficients of Cr, Ni, and Be agree with the experimental measurements within one order of magnitude, while those of Fe are within two orders of magnitude of the experimental measurements. The drag ratios for Cr, Fe, Be, and Ni are positive up to 1235 K, which suggests that nonequilibrium vacancy fluxes could drag these solutes toward sinks such as dislocation loops and grain boundaries. We also compute the transport coefficients without including the metastable states, and using the eight- and thirteen-frequency model. Our results show significant differences in drag ratio for the eight- and thirteen-frequency model predictions compared with the Green's function methodology, but smaller errors in the solute diffusivity. Combining interstitial and vacancy-mediated diffusivities, we predict the unusual result that increased vacancy concentration slows down solute diffusivity, while a sufficiently high vacancy concentration can change the dominant mechanism to an accelerated vacancy-mediated diffusion.

DOI: [10.1103/PhysRevMaterials.3.033402](https://doi.org/10.1103/PhysRevMaterials.3.033402)

I. INTRODUCTION

Zirconium alloys exhibit high corrosion resistance, structural stability, and low neutron absorption cross section, which makes them suitable as nuclear fuel cladding materials for light water power reactors at service temperatures [1]. The two common zirconium alloys used as cladding materials in light water power reactors are Zircaloy-2(Sn,Cr,Fe,Ni) and Zircaloy-4(Sn,Cr,Fe) [2]. The solutes Sn, Cr, Fe, and Ni are major alloying additions in the zirconium alloy claddings [2], and exposure of these alloys to neutron irradiation is known to cause a redistribution of alloying elements [3–7] with significant consequences to the corrosion performance of the alloy [6,8–11]. An understanding of the atomic-scale transport of point defects in Zr will provide a step forward for new alloy development with increased tolerance to radiation. Recent advances in computer processing speeds and

availability of massively parallel computing facilities have allowed density functional theory (DFT) simulations to determine the atomistic properties of point defects [12]. Combining DFT results with advanced diffusion models [13] helps connect the macroscopic properties with the complex interplay of processes that occur on an atomic scale [14–16]. For the present study, we focus on the four major alloying elements, as well as Be and Al in the HCP Zr matrix. Aluminum could potentially diffuse in to the Zr matrix from the Fe-Cr-Al alloy coatings being developed to improve the oxidation resistance of Zr [17]. Beryllium addition could also improve the oxidation resistance based on a recent computational study of Be stability in Zr surfaces [18].

First-principles studies have computed defect energies and migration barriers of vacancies [19–24], self-interstitials [25–27], and solute-vacancy complexes [28,29] in the Zr matrix; however, the information is insufficient to characterize solute-vacancy flux coupling and there are open issues such as the modeling of metastable vacancy configuration in Zr [22]. First-principles calculations have shown that group IV HCP metals such as Ti [30,31] and Zr [22] exhibit a double-humped basal vacancy migration barrier (cf., Fig. 1) through a

*ajain17@illinois.edu

†p.burr@unsw.edu.au

‡dtrinkle@illinois.edu

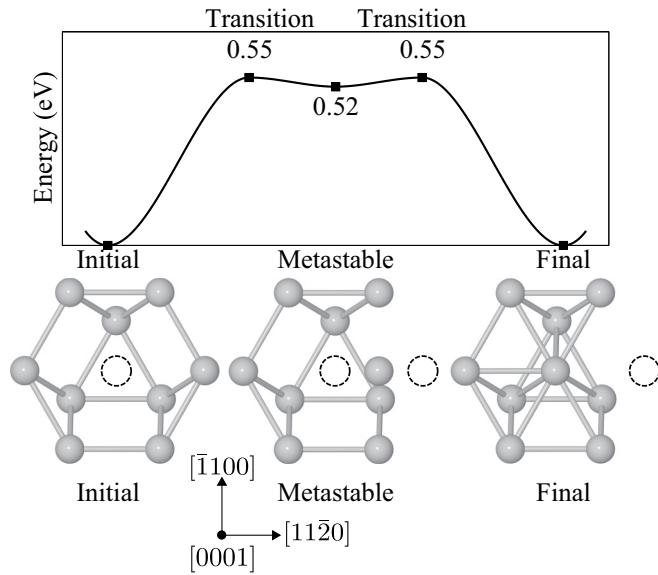


FIG. 1. Double-humped basal vacancy migration in HCP Zr. The metastable geometry of the vacancy in the 96-atom VASP calculation is 0.52 eV higher in energy than the ground state (lattice site) and located halfway between the initial and final positions. The transition state is 0.55 eV higher in energy than the ground state.

metastable configuration; however, previous investigations do not account for the metastable states [29,31,32] and assume that a vacancy directly transitions between lattice sites. Solute could either destabilize these states or form metastable solute-vacancy states [31], resulting in a complicated diffusion network, but existing diffusion models for HCP such as the eight-frequency model [33] and the thirteen-frequency model [34] are insufficient to capture such a network. A recent study [15,16] on vacancy-mediated diffusion in HCP Mg illustrated the use of an exact Green's function [13] (GF) approach that computes accurate transport coefficients for any arbitrary crystal, but there are no studies to validate the results of this approach for a system with metastable states.

The solutes Fe and Ni were shown to segregate toward grain boundaries in irradiated zirconium alloys [35,36] while Sn, Cr, Fe, and Ni form nanometer-sized clusters in the vicinity of dislocation loops [37–39]. In particular, Fe appears to cluster near (c) -type dislocation loops which are vacancy type [39], suggesting correlation between solute and vacancy fluxes. Segregation of solutes could be mediated by vacancies wherein the diffusion of vacancies toward sinks drags the solutes along; however, experimental measurements of diffusivity show that Cr [40,41], Fe [42,43], and Ni [43,44] are fast diffusers in the Zr matrix, and the interstitial mechanism is likely dominant under equilibrium conditions. On the other hand, the diffusivity of Sn in the Zr matrix [45] is similar to self-diffusion of Zr [46–50], suggesting a vacancy-mediated mechanism, but clustering of Sn appears to be anticorrelated with Fe and Cr [37,39] which suggests Sn and vacancy fluxes could also be anticorrelated.

First-principles studies also show that Fe [51,52] prefers interstitial sites over substitutional sites in HCP Zr. Pasianot *et al.* [53] performed first-principles calculations and found low migration barriers for Fe to jump between interstitial

sites, which could explain why Fe is a fast diffuser in the Zr matrix. In contrast, the solutes Cr [29,51], Be [18], and Ni [52] prefer substitutional sites in HCP Zr. Christensen *et al.*'s DFT study found that Fe and Cr have a low-energy substitutional configuration with a high magnetic moment and that Cr, Fe, and Ni have a weakly attractive binding with a vacancy in the first neighbor shell [28], which suggests a positive coupling between these solutes and vacancies. A recent study by Lu *et al.* [29] shows that vacancy has attractive binding with Cr but repulsive binding with Al and Sn, which suggests that the latter two solutes could be uncorrelated with vacancy fluxes; however, this correlation has not been quantified. The study also shows that Cr diffuses via the interstitial mechanism, which does not explain how solute-vacancy correlation could influence diffusion. There are currently no computational studies of diffusion coefficients of Fe, Be, and Ni in the Zr matrix. Further, the experimental measurements were carried out at near equilibrium conditions but the dominant diffusion mechanism can change under the effects of irradiation such as higher vacancy concentrations [54–57]. Thus, a combined study of both vacancy-mediated and interstitial diffusion mechanisms, along with their vacancy concentration dependence, can provide important quantitative data to model transport in zirconium alloys in equilibrium and radiation environments.

In this work, we extend a recently developed Green's function approach [13,58] to account for the metastable states and use it with inputs computed from DFT to examine vacancy and interstitial mediated diffusion of Sn, Cr, Fe, Be, Al, and Ni in the Zr matrix. We also perform kinetic Monte Carlo [59] (KMC) simulations for comparison with the results of the GF approach. In Sec. II, we discuss our unique treatment of the metastable vacancy states encountered in Zr and the definitions of solute-vacancy binding energies and transition rates. Section III describes the procedure for calculating the binding energies and transition rates from DFT. Section IV discusses the DFT results, the diffusion coefficients, and the drag ratios computed using the GF approach and KMC simulations. Our results show that the vacancy-mediated diffusion coefficients for Sn and Al are comparable to the experimental results. The interstitial diffusion coefficients computed using the GF approach and the competition between the interstitial and vacancy-mediated diffusion mechanisms. Our results show that the interstitial diffusion coefficients for Cr, Be, and Ni in HCP Zr agree to within one order of magnitude with the experimental results while those of Fe agree within two orders of magnitude. The drag ratios of Cr, Fe, Be, and Ni are positive, which suggests that vacancy fluxes at nonequilibrium concentrations retained due to irradiation damage could drag these solutes. We also predict that excess vacancies slow down the interstitial diffusion and accelerate vacancy-mediated diffusion.

II. METHODOLOGY

A. Vacancy-mediated transport

The Onsager transport coefficients [60] are second-rank tensors which describe the overall transport of point defects in alloys. In a binary alloy, the fluxes \vec{J}_S and \vec{J}_V of solute S and

vacancy V are proportional to the gradient of their chemical potentials μ_S and μ_V

$$\begin{pmatrix} \vec{J}_S \\ \vec{J}_V \end{pmatrix} = - \begin{pmatrix} L_{SS} & L_{SV} \\ L_{VS} & L_{VV} \end{pmatrix} \begin{pmatrix} \vec{\nabla} \mu_S \\ \vec{\nabla} \mu_V \end{pmatrix}, \quad (1)$$

where L_{SS} , $L_{SV} = L_{VS}$, and L_{VV} are the Onsager transport coefficients. In the dilute limit, the solute diffusivity D_S is proportional to L_{SS} ,

$$D_S = \lim_{c_S \rightarrow 0} \frac{k_B T}{c_S} L_{SS}, \quad (2)$$

where k_B is the Boltzmann constant, T is temperature in Kelvin, and c_S is the solute concentration. The term L_{SV} measures the correlation between solute and vacancy fluxes, and the drag ratio $L_{SV}(L_{SS})^{-1}$ quantifies the solute drag by vacancies. A positive drag ratio means that the vacancy drags the solute along with it while a negative value means that the solute diffuses away from the vacancy. Calculation of the transport coefficients requires identifying the set of states occupied by defects and the transition rates between these states. The following subsections discuss the definitions of these states and transition rates.

B. Solute-vacancy complexes in the dilute limit

We use the definition of a state introduced in the Green's function methodology [13] and extend it to include the description of the metastable states observed in HCP Zr. We consider an infinite three-dimensional lattice containing N sites in the unit cell ($i = 1 \dots N$), with the basis vectors \mathbf{u}_i . We define each site with the position vector $\mathbf{R} = \mathbf{x} + \mathbf{u}_i$, where \mathbf{x} is a linear combination of the unit cell lattice vectors. Then the position of a solute is $\mathbf{x}_S + \mathbf{u}_{i_S}$, and the position of a vacancy at a lattice site relative to the solute is $\mathbf{x}_S + \mathbf{x}_V + \mathbf{u}_{i_V}$. Therefore, we can represent a solute-vacancy complex state as $\mathbf{x}_S i_S \mathbf{x}_V i_V$ when the vacancy occupies a lattice site. In the case of metastable complex states, the vacancy does not occupy a lattice site; instead, two lattice sites are simultaneously occupied by "half vacancies" and we use two adjacent vacancy positions $\mathbf{x}_V i_V$ and $\mathbf{y}_V j_V$ to define a metastable complex state as $\mathbf{x}_S i_S \mathbf{x}_V i_V \mathbf{y}_V j_V$. In the dilute limit, we consider only one solute and one vacancy in the system, and set $\mathbf{x}_S = \mathbf{0}$ using the translational invariance of the lattice. Therefore, the set of states can be represented by $\mathbf{0} i_S \mathbf{x}_V i_V$ and $\mathbf{0} i_S \mathbf{x}_V i_V \mathbf{y}_V j_V$. Note that the states $\mathbf{0} i_S \mathbf{x}_V i_V \mathbf{y}_V j_V$ and states $\mathbf{0} i_S \mathbf{y}_V j_V \mathbf{x}_V i_V$ are equivalent.

We determine the thermodynamic range of interaction between the solute and vacancy using the solute-vacancy binding energies $E_{\mathbf{0} i_S \mathbf{x}_V i_V}^b$ and $E_{\mathbf{0} i_S \mathbf{x}_V i_V \mathbf{y}_V j_V}^b$ for a vacancy occupying a lattice site and metastable state, respectively. We assume that the thermodynamic range is finite, and the vacancy state and transition state energies are independent of the solute beyond this range. We define the binding energies relative to the energy $E_{\mathbf{0} i_S}$ of a single solute in the system without the vacancy, and energy $E_{\mathbf{0} i_V}$ of a single vacancy at a lattice site without the solute in the system

$$E_{\mathbf{0} i_S \mathbf{x}_V i_V}^b = E_{\mathbf{0} i_S \mathbf{x}_V i_V} - (E_{\mathbf{0} i_S} + E_{\mathbf{0} i_V}), \quad (3)$$

$$E_{\mathbf{0} i_S \mathbf{x}_V i_V \mathbf{y}_V j_V}^b = E_{\mathbf{0} i_S \mathbf{x}_V i_V \mathbf{y}_V j_V} - (E_{\mathbf{0} i_S} + E_{\mathbf{0} i_V}), \quad (4)$$

where $E_{\mathbf{0} i_S \mathbf{x}_V i_V}$ is the energy of the complex $\mathbf{0} i_S \mathbf{x}_V i_V$ and $E_{\mathbf{0} i_S \mathbf{x}_V i_V \mathbf{y}_V j_V}$ is the energy of the metastable complex $\mathbf{0} i_S \mathbf{x}_V i_V \mathbf{y}_V j_V$. The binding energy decays to zero as the separation between the solute and vacancy approaches the thermodynamic range. Based on the chosen reference, if the vacancy occupies any metastable state outside the thermodynamic range, then $E_{\mathbf{0} i_S \mathbf{x}_V i_V \mathbf{y}_V j_V}^b$ reduces to the relative energy of metastable state without the solute: $E_{\mathbf{0} i_V \mathbf{y}_V j_V} - E_{\mathbf{0} i_V}$. We define a positive binding energy as repulsive interactions while a negative binding energy denotes attractive interactions.

C. Transition rates

The minimum energy transition pathway between two states goes through a saddle-point configuration in the potential energy surface and we use the harmonic transition state theory [61] to compute the transition rate. We refer to the saddle-point configuration as the transition state, and its location along the minimum energy path as the reaction coordinate. The transition rate $\omega_{\mathbf{0} i_S \mathbf{x}_V i_V - \mathbf{x}'_S i'_S \mathbf{x}'_V i'_V}$ between the initial state $\mathbf{0} i_S \mathbf{x}_V i_V$ and the final state $\mathbf{x}'_S i'_S \mathbf{x}'_V i'_V$ is then

$$\omega_{\mathbf{0} i_S \mathbf{x}_V i_V - \mathbf{x}'_S i'_S \mathbf{x}'_V i'_V} = \nu_{\mathbf{0} i_S \mathbf{x}_V i_V - \mathbf{x}'_S i'_S \mathbf{x}'_V i'_V} e^{-E_{\mathbf{0} i_S \mathbf{x}_V i_V - \mathbf{x}'_S i'_S \mathbf{x}'_V i'_V}^m / k_B T}, \quad (5)$$

where $\nu_{\mathbf{0} i_S \mathbf{x}_V i_V - \mathbf{x}'_S i'_S \mathbf{x}'_V i'_V}$ is the attempt frequency and $E_{\mathbf{0} i_S \mathbf{x}_V i_V - \mathbf{x}'_S i'_S \mathbf{x}'_V i'_V}^m$ is the migration energy. The migration energy $E_{\mathbf{0} i_S \mathbf{x}_V i_V - \mathbf{x}'_S i'_S \mathbf{x}'_V i'_V}^m$ is

$$E_{\mathbf{0} i_S \mathbf{x}_V i_V - \mathbf{x}'_S i'_S \mathbf{x}'_V i'_V}^m = E_{\mathbf{0} i_S \mathbf{x}_V i_V - \mathbf{x}'_S i'_S \mathbf{x}'_V i'_V}^T - E_{\mathbf{0} i_S \mathbf{x}_V i_V}, \quad (6)$$

where $E_{\mathbf{0} i_S \mathbf{x}_V i_V - \mathbf{x}'_S i'_S \mathbf{x}'_V i'_V}^T$ is the energy of the transition state. Similarly, the transition rate $\omega_{\mathbf{0} i_S \mathbf{x}_V i_V - \mathbf{0} i_S \mathbf{x}_V i_V \mathbf{y}_V j_V}$ between the initial state $\mathbf{0} i_S \mathbf{x}_V i_V$ and the metastable state $\mathbf{0} i_S \mathbf{x}_V i_V \mathbf{y}_V j_V$ is

$$\omega_{\mathbf{0} i_S \mathbf{x}_V i_V - \mathbf{0} i_S \mathbf{x}_V i_V \mathbf{y}_V j_V} = \nu_{\mathbf{0} i_S \mathbf{x}_V i_V - \mathbf{0} i_S \mathbf{x}_V i_V \mathbf{y}_V j_V} e^{-E_{\mathbf{0} i_S \mathbf{x}_V i_V - \mathbf{0} i_S \mathbf{x}_V i_V \mathbf{y}_V j_V}^m / k_B T}. \quad (7)$$

We assume that the vacancy at a metastable state only transitions to the adjacent lattice sites. Note that the transition states $\mathbf{0} i_S \mathbf{x}_V i_V - \mathbf{0} i_S \mathbf{x}_V i_V \mathbf{y}_V j_V$ and $\mathbf{0} i_S \mathbf{x}_V i_V \mathbf{y}_V j_V - \mathbf{0} i_S \mathbf{x}_V i_V$ are equivalent, but different from $\mathbf{0} i_S \mathbf{y}_V j_V - \mathbf{0} i_S \mathbf{x}_V i_V \mathbf{y}_V j_V$ or $\mathbf{0} i_S \mathbf{x}_V i_V \mathbf{y}_V j_V - \mathbf{0} i_S \mathbf{y}_V j_V$.

The combined effect of various transition rates governs the solute transport kinetics via the vacancy-mediated mechanism. Vacancy-mediated diffusion of solutes requires solute-vacancy exchange jumps followed by reorientation jumps of vacancy around the solute. Therefore, the solute diffusion coefficient depends on the rate-limiting step between exchange and reorientation. Solute drag occurs when the solute and the vacancy diffuse as a complex. Attractive binding energies increase the probability that vacancies migrate toward the solute and form complexes. Alternatively, drag is also possible when binding energies are repulsive, provided that the vacancy reorientation rates around the solute are much faster than the rates to escape away from the solute, which increases the probability that solute and vacancy diffuse as a complex.

Calculating the interstitial diffusion coefficient requires identifying the set of interstitial sites and the transition rates between them. In the dilute limit, we consider only one solute diffusing in the system. Therefore, we use the translational

invariance of the system to describe the complete set of states using only the interstitial sites located in the unit cell. We use harmonic transition state theory [61] to compute the transition rate $\omega_{\alpha-\beta}$ for an interstitial to jump from a site α to another site β . The minimum energy path for this jump passes through a transition state $\alpha-\beta$. The transition rate $\omega_{\alpha-\beta}$ is

$$\omega_{\alpha-\beta} = \nu_{\alpha-\beta} e^{-E_{\alpha-\beta}^m/k_B T}, \quad (8)$$

where $\nu_{\alpha-\beta}$ is the attempt frequency and $E_{\alpha-\beta}^m$ is the migration energy. The migration energy $E_{\alpha-\beta}^m$ is

$$E_{\alpha-\beta}^m = E_{\alpha-\beta}^T - E_{\alpha}, \quad (9)$$

where $E_{\alpha-\beta}^T$ is the energy of the transition state and E_{α} is the energy of the initial site.

III. COMPUTATIONAL DETAILS

We perform density functional theory (DFT) calculations using the Perdew-Burke-Ernzerhof (PBE) exchange-correlation functional [62] and the projector augmented wave (PAW) method [63] implemented in the Vienna *ab initio* simulation package (VASP) [64,65]. We describe the Zr, Sn, Cr, Fe, Be, Al, and Ni atoms with the electronic configurations [Kr]4d²5s², [Kr]4d¹⁰5s²5p², [Ar]3d⁵4s¹, [Ar]3d⁶4s², [He]2s², [Ne]3s²3p¹, and [Ar]3d⁸4s², respectively. We use a plane-wave energy cutoff of 500 eV to converge the total energy of Zr below 1 meV per atom. We use a supercell of size 4 × 4 × 3 (96 atoms) which requires a Monkhorst-Pack [66] *k*-point mesh size of 6 × 6 × 4 to sample the Brillouin zone. We use Methfessel-Paxton smearing [65] with an energy smearing width of 0.2 eV to integrate the density of states. The convergence criterion for electronic minimization is an energy difference smaller than 10⁻⁸ eV. We relax the geometries using conjugate gradient until the force on each atom is less than 5 meV/Å. We use spin polarization for the calculations involving Cr and Fe, because the ground-state substitutional configurations of these solutes have magnetic moments of 3.82 μ_B and 3.62 μ_B respectively. We use the climbing image nudged elastic band (NEB) method [67] with a single image to determine the transition states for vacancy jumps. The lattice constants for HCP Zr obtained from structural relaxation are $a = 3.234$ Å and $c = 5.171$ Å, which agree well with experimental data [68] and previous DFT studies [69,70]. The calculated vacancy formation energy in Zr is 2 eV, which is comparable to other DFT results reported in the literature [22,32,70–72]. The experimental measurements [47,73] estimate that the lower bound for vacancy formation energy is 1.5 eV; however, accurate measurements are not available. The vacancy formation energies computed using the Zr PAW potentials with 4 valence electrons and 12 valence electrons differ by less than 20 meV. We performed spin-polarized calculations for cells containing Fe, but we find that all interstitial configurations have a zero magnetic moment.

We compute total energies of Zr supercells containing a single solute atom in various interstitial sites and transition-state geometries and use these energies to calculate the defect formation energies and migration barriers, respectively. The formation energy E_{α}^f of a single solute atom S at the interstitial

site α in the Zr lattice is

$$E_{\alpha}^f = E^{\text{DFT}}[S_{\alpha} + (M)\text{Zr}] - E^{\text{DFT}}[(M)\text{Zr}] - E^{\text{DFT}}[S], \quad (10)$$

where $E^{\text{DFT}}[S_{\alpha} + (M)\text{Zr}]$ is the DFT energy of the supercell containing a solute at the interstitial site α and M Zr atoms, $E^{\text{DFT}}[(M)\text{Zr}]$ is the DFT energy of the supercell containing M Zr atoms, and $E^{\text{DFT}}[S]$ is the DFT energy of an isolated solute atom. For the 4 × 4 × 3 bulk supercell, M is 96. We set the lowest energy site as the reference and report the energies of all other sites relative to this reference. As a result, the last two terms in Eq. (10) cancel out. We calculate the migration energy $E_{\alpha-\beta}^m$ as

$$E_{\alpha-\beta}^m = E^{\text{DFT}}[S_{\alpha-\beta} + (M)\text{Zr}] - E^{\text{DFT}}[S_{\alpha} + (M)\text{Zr}], \quad (11)$$

where $E^{\text{DFT}}[S_{\alpha-\beta} + (M)\text{Zr}]$ is the DFT energy of the transition state between the sites α and β .

For solute vacancy complexes and associated transition states, we use DFT supercells of the same size ($M = 96$) to determine the energies $E^{\text{DFT}}[(M-1)\text{Zr}+i_S]$ of Zr containing a single substitutional solute, $E^{\text{DFT}}[(M-1)\text{Zr}+i_V]$ of Zr containing a single vacancy, and $E^{\text{DFT}}[(M-2)\text{Zr}+\mathbf{0}_i\mathbf{x}_V\mathbf{y}_V]$ of Zr containing the solute-vacancy complex. The binding energy $E_{\mathbf{0}_i\mathbf{x}_V\mathbf{y}_V}^b$ of the solute-vacancy complex state $\mathbf{0}_i\mathbf{x}_V\mathbf{y}_V$ from DFT is then

$$\begin{aligned} E_{\mathbf{0}_i\mathbf{x}_V\mathbf{y}_V}^b &= E^{\text{DFT}}[(M-2)\text{Zr} + \mathbf{0}_i\mathbf{x}_V\mathbf{y}_V] \\ &\quad - (E^{\text{DFT}}[(M-1)\text{Zr} + i_S] \\ &\quad + E^{\text{DFT}}[(M-1)\text{Zr} + i_V]) \\ &\quad - E^{\text{DFT}}[(M)\text{Zr}], \end{aligned} \quad (12)$$

where the term $E^{\text{DFT}}[(M)\text{Zr}]$ on the right-hand side balances the DFT energy of M Zr atoms. Similarly, the binding energy $E_{\mathbf{0}_i\mathbf{x}_V\mathbf{y}_V\mathbf{y}_V}^b$ of the metastable state $\mathbf{0}_i\mathbf{x}_V\mathbf{y}_V\mathbf{y}_V$ is

$$\begin{aligned} E_{\mathbf{0}_i\mathbf{x}_V\mathbf{y}_V\mathbf{y}_V}^b &= E^{\text{DFT}}[(M-2)\text{Zr} + \mathbf{0}_i\mathbf{x}_V\mathbf{y}_V\mathbf{y}_V] \\ &\quad - \{E^{\text{DFT}}[(M-1)\text{Zr} + i_S] \\ &\quad + E^{\text{DFT}}[(M-1)\text{Zr} + i_V]\} \\ &\quad - E^{\text{DFT}}[(M)\text{Zr}], \end{aligned} \quad (13)$$

where $E^{\text{DFT}}[(M-2)\text{Zr} + \mathbf{0}_i\mathbf{x}_V\mathbf{y}_V\mathbf{y}_V]$ is the DFT energy of the metastable state $\mathbf{0}_i\mathbf{x}_V\mathbf{y}_V\mathbf{y}_V$. The migration energy $E_{\mathbf{0}_i\mathbf{x}_V\mathbf{y}_V-\mathbf{x}'_S\mathbf{i}'_S\mathbf{x}'_V\mathbf{i}'_V}^m$ for a vacancy jump between states $\mathbf{0}_i\mathbf{x}_V\mathbf{y}_V$ and $\mathbf{x}'_S\mathbf{i}'_S\mathbf{x}'_V\mathbf{i}'_V$ is

$$\begin{aligned} E_{\mathbf{0}_i\mathbf{x}_V\mathbf{y}_V-\mathbf{x}'_S\mathbf{i}'_S\mathbf{x}'_V\mathbf{i}'_V}^m &= E^{\text{T,DFT}}[(M-2)\text{Zr} \\ &\quad + \mathbf{0}_i\mathbf{x}_V\mathbf{y}_V - \mathbf{x}'_S\mathbf{i}'_S\mathbf{x}'_V\mathbf{i}'_V] \\ &\quad - E^{\text{DFT}}[(M-2)\text{Zr} + \mathbf{0}_i\mathbf{x}_V\mathbf{y}_V], \end{aligned} \quad (14)$$

where $E^{\text{T,DFT}}[(M-2)\text{Zr} + \mathbf{0}_i\mathbf{x}_V\mathbf{y}_V - \mathbf{x}'_S\mathbf{i}'_S\mathbf{x}'_V\mathbf{i}'_V]$ is the DFT energy of the transition state between the states $\mathbf{0}_i\mathbf{x}_V\mathbf{y}_V$ and $\mathbf{x}'_S\mathbf{i}'_S\mathbf{x}'_V\mathbf{i}'_V$. The migration energy between a state $\mathbf{0}_i\mathbf{x}_V\mathbf{y}_V$ and a metastable state $\mathbf{0}_i\mathbf{x}_V\mathbf{y}_V\mathbf{y}_V$ is given by a similar expression.

We compute the vibrational frequencies of the jumping atom in the initial state and transition state from DFT, and use these frequencies to determine the attempt frequencies. We approximate the Vineyard expression [61] of the attempt

frequency for interstitial transitions as

$$\nu_{\alpha-\beta} = \frac{\prod_{l=1}^3 \nu_{\alpha,l}^*}{\prod_{l=1}^2 \nu_{\alpha-\beta,l}^*}, \quad (15)$$

where $\nu_{\alpha,l}^*$ are the vibrational frequencies of the interstitial atom at site α and $\nu_{\alpha-\beta,l}^*$ are the real vibrational frequencies of the interstitial atom in transition state $\alpha-\beta$. For vacancy-mediated transitions, we find

$$\nu_{\mathbf{0}_{i_S \mathbf{x}_{V i_V} - \mathbf{x}'_S i'_S \mathbf{x}'_V i'_V}} = \frac{\prod_{l=1}^3 \nu_{\mathbf{0}_{i_S \mathbf{x}_{V i_V}, l}^*}}{\prod_{l=1}^2 \nu_{\mathbf{0}_{i_S \mathbf{x}_{V i_V} - \mathbf{x}'_S i'_S \mathbf{x}'_V i'_V, l}^*}}, \quad (16)$$

where $\nu_{\mathbf{0}_{i_S \mathbf{x}_{V i_V}, l}^*}$ are the vibrational frequencies of the jumping atom in state $\mathbf{0}_{i_S \mathbf{x}_{V i_V}}$ and $\nu_{\mathbf{0}_{i_S \mathbf{x}_{V i_V} - \mathbf{x}'_S i'_S \mathbf{x}'_V i'_V, l}^*}$ are the real vibrational frequencies of the moving atom in transition state $\mathbf{0}_{i_S \mathbf{x}_{V i_V} - \mathbf{x}'_S i'_S \mathbf{x}'_V i'_V}$. We determine the vibrational frequencies from the eigenvalues of the force constant matrix, by displacing the jumping atom by small amounts (± 0.01 Å) along three orthogonal directions and calculating the resulting forces. Similar procedure applies for the transitions between a lattice site and a metastable state.

The linearly interpolated migration barrier (LIMB) approximation uses the transition-state energies for vacancy migration without the solute and the solute-vacancy binding energies to approximate the transition-state energies in the presence of the solute. The results from the LIMB approximation improve for the vacancy transitions which are further away from the solute because the energy landscape becomes similar to bulk. Computing a large number of transition-state energies using DFT is expensive; therefore, we use LIMB to approximate the transition-state energies for vacancy jumps away from the nearest neighbor shell of solutes which limits

the number of DFT calculations. The LIMB approximation for the transition-state energy of a vacancy jump between two lattice sites is

$$E_{\mathbf{0}_{i_S \mathbf{x}_{V i_V} - \mathbf{x}'_S i'_S \mathbf{x}'_V i'_V}}^{\text{T, LIMB}} = (1-r)E_{\mathbf{0}_{i_S \mathbf{x}_{V i_V}}} + rE_{\mathbf{x}'_S i'_S \mathbf{x}'_V i'_V} + [E_{\mathbf{0}_{i_V - \mathbf{x}'_V i'_V}}^{\text{T}} - (1-r)E_{\mathbf{0}_{i_V}} - rE_{\mathbf{x}'_V i'_V}], \quad (17)$$

where $E_{\mathbf{0}_{i_V - \mathbf{x}'_V i'_V}}^{\text{T}}$ is the transition-state energy for a vacancy jump without a solute and $0 \leq r \leq 1$ is the reaction coordinate of the transition state relative to the initial state. Similarly, the LIMB approximation for the transition-state energy of a vacancy jump between a lattice site and a metastable state is

$$E_{\mathbf{0}_{i_S \mathbf{x}_{V i_V} - \mathbf{0}_{i_S \mathbf{x}_{V i_V} \mathbf{y}_V \mathbf{j}_V}}^{\text{T, LIMB}}} = (1-r)E_{\mathbf{0}_{i_S \mathbf{x}_{V i_V}}} + rE_{\mathbf{0}_{i_S \mathbf{x}_{V i_V} \mathbf{y}_V \mathbf{j}_V}} + [E_{\mathbf{0}_{i_V - \mathbf{0}_{i_V \mathbf{y}_V \mathbf{j}_V}}^{\text{T}}} - (1-r)E_{\mathbf{0}_{i_V}} - rE_{\mathbf{0}_{i_V \mathbf{y}_V \mathbf{j}_V}}], \quad (18)$$

where $E_{\mathbf{0}_{i_V - \mathbf{0}_{i_V \mathbf{y}_V \mathbf{j}_V}}^{\text{T}}}$ is the transition-state energy for a vacancy jump without a solute between a lattice site and a metastable state.

IV. RESULTS

A. Vacancy migration in bulk Zr

Figure 1 illustrates the geometries of a single vacancy at a lattice site in HCP Zr and the metastable state located along the basal transition path, which is 0.52 eV higher in energy. The vacancy transitions between a lattice site and metastable state via basal jumps along $\langle 11\bar{2}0 \rangle$ directions and between two lattice sites via pyramidal jumps along $\langle 02\bar{2}3 \rangle$ direction. The basal migration barrier computed from DFT is 0.553 eV

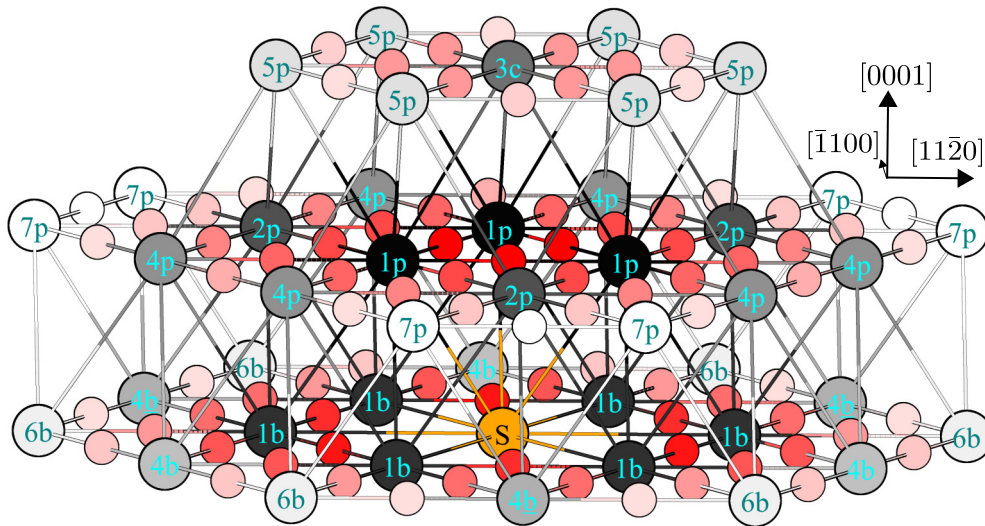


FIG. 2. The solute-vacancy complex configurations up to the seventh neighbor shell in HCP Zr. The large spheres mark the lattice sites and the small spheres mark the metastable states. The numbers 1–7 correspond to the successive neighbor shells of an ideal HCP lattice with c/a ratio = $\sqrt{8/3}$. The letters b, p and c denote basal, pyramidal, and c -axis neighbors, respectively. The darker colors are closer to the solute and lighter colors are further away. There are six 1b, three 4b and 4 \bar{b} , and six 6b sites in the basal plane of the solute; six 1p, six 2p, twelve 4p, and twelve 7p sites, located one plane above and below the plane of solute; and two 3c and twelve 5p sites located two planes above and below the plane of the solute atom. The sites 4b and 4 \bar{b} are equidistant from the solute but nonequivalent by symmetry. The neighbors below the basal plane of the solute atom are located at symmetric positions along the c axis (not shown). No metastable state exists between the solute and the 1b neighbors.

and the reaction coordinate of the transition state is located at $r = 2/3$. Therefore, the vacancy undergoes a basal transition between two lattice sites via a double-humped barrier. The pyramidal migration barrier is 0.613 eV, and the reaction coordinate is located at $r = 1/2$. The attempt frequency for basal jumps and pyramidal jumps out of a lattice site are 5.205 and 5.849 THz, respectively. The attempt frequency for a jump out of the metastable state is 1.758 THz. Our results are comparable to the vacancy migration barriers from DFT calculations reported in the literature: 0.51 [22], 0.54 [70], 0.57 [72], 0.5 [32], and 0.55 [32] eV for the basal jumps and 0.67 [22], 0.65 [70], 0.70 [72], 0.53 [32], and 0.62 [32] eV for the pyramidal jump. To simplify the description of metastable states, we choose to map the metastable states onto a sublattice of sites located between the lattice sites and use this mapping in our GF calculations. Therefore, our HCP unit cell includes six additional symmetry-equivalent basis sites which have the same symmetry and Wyckoff positions as the basal crowdion sites.

B. Solute-vacancy complexes

Figure 2 illustrates the various possible solute-vacancy complexes when the vacancy occupies the lattice sites or metastable states around a solute atom, up to the seventh neighbor shell in HCP Zr. The lattice sites and their multiplicities (in parentheses) in increasing order of distance from the solute for an ideal HCP lattice are: 1p (6), 1b (6), 2p (6), 3c (2), 4p (12), 4b (3) and $\underline{4b}$ (3), 5p (12), 6b (6), and 7p (12). Note that the sites 4b and $\underline{4b}$ are at the same distance in the unrelaxed geometry but they are symmetrically nonequivalent and relax independently when a solute is introduced. There is a metastable state between any two neighboring lattice sites on the same basal plane, except between the solute (S) and 1b. We label these metastable states using the labels of the neighboring lattice sites; for example, the metastable state connecting 2p and 4p is 2p4p. There are two sets of symmetrically nonequivalent metastable states located along [01 $\bar{1}$ 0] and [$\bar{1}$ 100], which connect the 1b sites, and we label these states

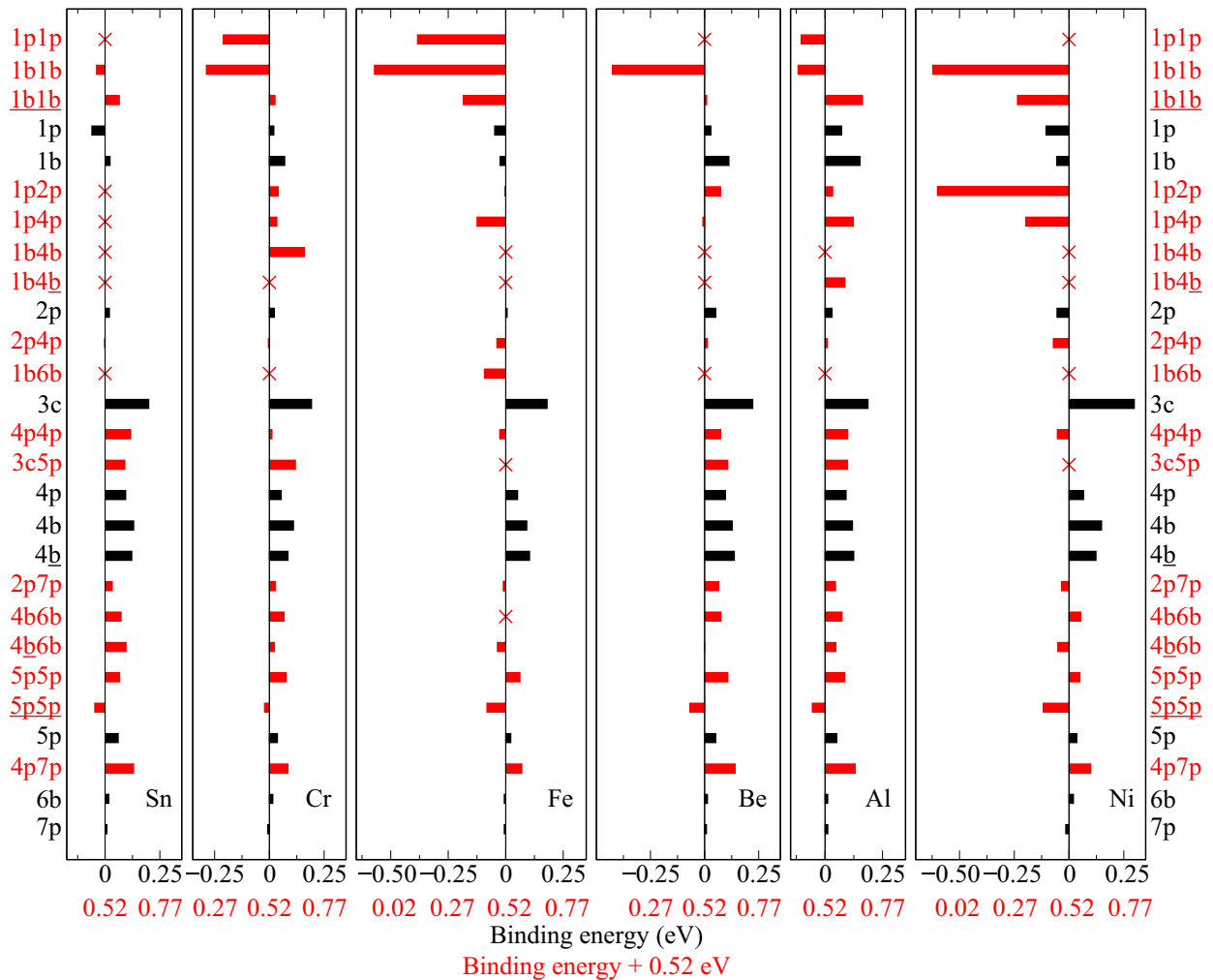


FIG. 3. Binding energies of the solute-vacancy complexes shown in Fig. 2 calculated using Eq. (12) for Sn, Cr, Fe, Be, Al, and Ni. The black bars and the black horizontal scale measure the binding energies between a solute and a vacancy at lattice sites, while the red bars and red scale are for metastable states. We shift the red scale by 0.52 eV, which is the difference between the energy of a vacancy in bulk metastable configuration and the energy of a vacancy in the ground-state configuration. The red cross indicates if there is no metastable state. For all solutes, 3c has the largest repulsive binding energy among the lattice sites. The metastable state 1b1b for Fe, Be, and Ni has lower binding energies than the lattice sites.

TABLE I. Attempt frequencies (ν_{xp} and ν_{xb}) in THz and migration barriers (E_{xp}^m and E_{xb}^m) in eV computed from DFT for solute-vacancy pyramidal and basal exchange jumps. The reference energy is the corresponding site energy, that is, 1b for a basal exchange and 1p for a pyramidal exchange.

Solute	Pyramidal		Basal	
	ν_{xp}	E_{xp}^m	ν_{xb}	E_{xb}^m
Sn	3.409	0.992	3.300	0.764
Cr	3.116	0.751	4.507	0.680
Fe	3.664	0.637	3.852	0.632
Be	0.835	0.963	0.916	0.834
Al	0.989	1.057	1.012	0.905
Ni	4.275	0.712	11.247	0.657

as 1b1b and $\underline{1b1b}$ respectively. The same distinction applies to the metastable states $5p5p$ and $\underline{5p5p}$ connecting the 5p sites as well. Note that these sites are equivalent for vacancy migration in bulk but the presence of both a solute and a vacancy lowers the symmetry of the system, thus introducing nonequivalent configurations. Previous computational studies of diffusion in HCP systems have neglected the difference between 1b1b and $\underline{1b1b}$ jumps [29,31–34], which was first shown by Agarwal *et al.* [15] and here again we show that these jumps have significantly different characteristics. The metastable states and their multiplicities (in parentheses) in increasing order of distance from the solute are 1p1p (6), 1b1b (3) and $\underline{1b1b}$ (3), 1p2p (12), 1p4p (12), 1b4b (6) and $\underline{1b4b}$ (6), 2p4p (12), 1b6b (6), 4p4p (6), 3c5p (12), 2p7p (12), 4b6b (6) and $\underline{4b6b}$ (6), $5p5p$ (6) and $\underline{5p5p}$ (6), and 4p7p (12). A complete description of the mapping between our simplified state labels and the mathematical description of states is presented in the Table V.

Figure 3 shows the binding energies computed using Eq. (12) for all the complex configurations shown in Fig. 2, indicating that the solute-vacancy interactions are non-negligible up to the fifth neighbor shell. Every solute exhibits cases where there are no metastable states (marked by a red \times), most notable for Sn where there are no metastable states between the nearest neighbors and next nearest neighbors, except for 1b1b and $\underline{1b1b}$. We find attractive binding with the vacancy in the first and second shells for Sn, Fe, and Ni. Tin shows repulsive binding with the vacancy at 1b and 2p, while Cr, Be, and Al have repulsive binding energies at all lattice sites. The site 3c has the largest repulsive binding among lattice sites for all solutes. In addition, the metastable complex 1b1b for Fe, Be, and Ni have the strongest binding, which makes them the lowest energy configurations for these systems, and we expect strong correlations between these solutes and the vacancy. The geometries of these low-energy 1b1b complexes are particularly unusual as the moving Zr atom displaces close to the solute due to the attractive binding (cf., Fig. 18). The binding energies at the sites 6b and 7p become negligible for all solutes, so we consider these outside the interaction range and set their binding energies to zero in our calculations.

Table I shows that the migration barriers for pyramidal exchange are considerably larger than basal exchange for all solutes except Fe, where they are comparable. Therefore, we

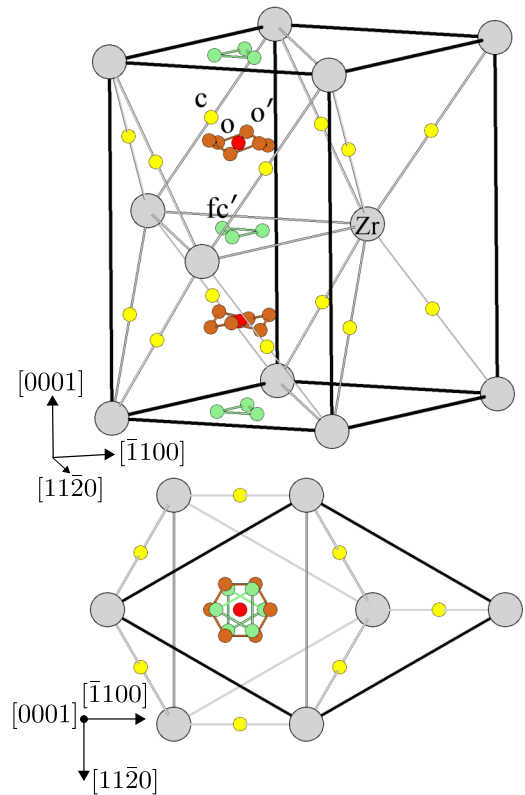


FIG. 4. The side view (top) and the (0001) plane projection (bottom) of the HCP Zr lattice showing the interstitial sites for Cr, Fe, Be, and Ni solutes. The Zr matrix atoms are in light gray, octahedral (o) sites are in red, the crowdion sites (c) are in yellow, the distorted face center sites (fc') are in light green, and the off-centered octahedral sites (o') are in dark orange. In the two-atom unit cell of HCP Zr, there are two o, six c, six fc' , and twelve o' sites. The set of o' sites are displaced away from the o site at symmetric positions. The Wyckoff letters for the sites o, c, fc' , and o' corresponding to the $P6_3/mmc$ group are a, g, h, and k, respectively.

expect isotropic diffusion for Fe and anisotropic behavior for all other solutes. Moreover, the barriers are consistently higher than the bulk vacancy diffusion barriers, which suggests that the exchange barrier is the rate-limiting step for diffusion and we expect the activation barriers for diffusion of these solutes to be higher than self-diffusion in Zr. Iron is the only exception where the pyramidal exchange is faster than the bulk diffusion barrier. We have also listed the corresponding attempt frequencies, and these values show the largest deviations from the bulk attempt frequencies for all solutes, as compared to other vacancy jumps, which are away from the solute. Our results for Sn, Cr, and Al agree well with those reported in a recent study on diffusion in Zr [29].

C. Interstitial positions

Figure 4 illustrates the relative positions of all the stable interstitial sites that we find for the solutes Cr, Fe, Be, and Ni in the HCP Zr lattice. There are six off-centered octahedral o' sites located around the octahedral o site. Similarly, there are three distorted face-center fc' sites located in the basal plane between the two o sites. We find that the o and o' sites are

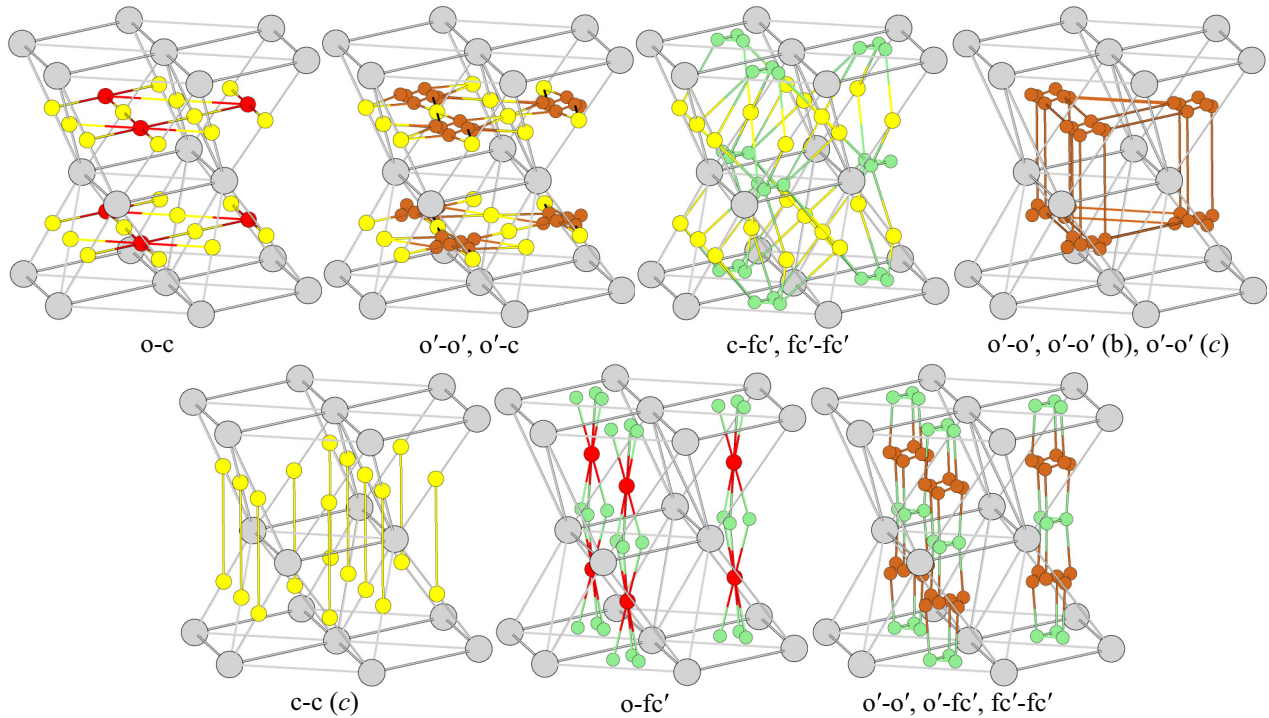


FIG. 5. The networks of interstitial sites for Cr, Fe, Be, and Ni solutes in HCP Zr. The first two networks in the top row contribute only to basal diffusion while the next two contribute to both c axis and basal diffusion. The three networks in the bottom row contribute only to c -axis diffusion. In the cases where a jump starts and ends at the same type of site (such as $o'-o'$), we distinguish the diffusive jump as (b) for a basal jump and (c) for a c -axis jump.

never simultaneously stable for the same solute. Chromium is stable at o (lowest energy), fc' , and c . Iron is stable at o' (lowest energy), c , and fc' . We previously reported that Be occupies an octahedral interstitial site in Zr [18] but find that upon displacement, the octahedral site relaxes to an o' geometry. Ni is stable at o' (lowest energy) and fc' . In addition, the lowest energy interstitial sites for Cr, Be, and Ni are higher in energy relative to the substitutional sites by 0.80, 0.63, and 0.23 eV, respectively. Iron prefers the o' site to the substitutional site by 0.21 eV. Note that the lowest energy substitutional Cr and Fe configurations have a nonzero magnetic moment of $3.82 \mu_B$ and $3.62 \mu_B$, respectively. Further, we find that non-spin-polarized calculations increase the energy of the substitutional Cr and Fe configurations by 0.77 and 0.57 eV, respectively. However, the magnetic moment of all interstitial sites is zero even with spin-polarized calculations.

The seven possible diffusion networks in Fig. 5, formed from the stable interstitial sites in Fig. 4, have different contributions to diffusion in the basal plane and along the c axis. The first network between o sites and c sites contributes to the basal diffusion of Cr. The second network has two connections: $o'-o'$ and $o'-c$, where the former leads to transitions within the set of o' sites in the same unit cell and the latter contributes to the basal diffusion of Fe. The third network also has two connections, $fc'-fc'$ and $fc'-c$, where the former leads to transitions within the set of fc' sites in the same unit cell and the latter contributes to both basal and c -axis diffusion of Fe. The fourth network has three connections between the o' sites: transitions within the same unit cell, the basal connection (b), and the c -axis connection (c). The basal connection between

o' sites contributes to the basal diffusion of Be and Ni, while the c -axis connection contributes to the c -axis diffusion of Be. The fifth network between c sites contributes to the c -axis diffusion of Cr. The sixth network between o sites and fc' sites also contributes to the c -axis diffusion of Cr. The seventh network has three connections: $o'-o'$, $o'-fc'$, and $fc'-fc'$, where the $o'-fc'$ connection contributes to the c axis diffusion of Fe and Ni.

Figure 6 depicts the energies of all stable interstitial sites and transition states for Cr, Fe, Be and Ni solutes in Zr, which determines the dominant diffusion pathways. For Cr, the $o-c$ and $o-fc'$ are the dominant contributions to basal and c -axis diffusion, respectively, with the c -axis jump being faster. For Fe, the $o'-o'$ and $fc'-fc'$ jumps are nondiffusive while the $o'-c$ and $o'-fc'$ jumps which have similar migration barriers contribute to basal and c -axis diffusion. Beryllium is only stable at o' and both basal (b) and c -axis (c) diffusive jumps are between the o' sites, with the basal jump being faster. For Ni, the $o'-o'$ (b) and $o'-fc'$ jumps contribute to the basal and c -axis diffusion, respectively, and we expect faster diffusion along the c axis because of the lower migration barrier.

D. Diffusion coefficients and drag ratios

Figure 7 shows that the vacancy-mediated diffusion coefficients of Sn and Al are comparable to the experimental data [45,74], and there is good agreement between GF calculations and KMC results. Since the two methods give almost identical results, we compute the results for Al and Ni using only the GF method, which is faster and more accurate.

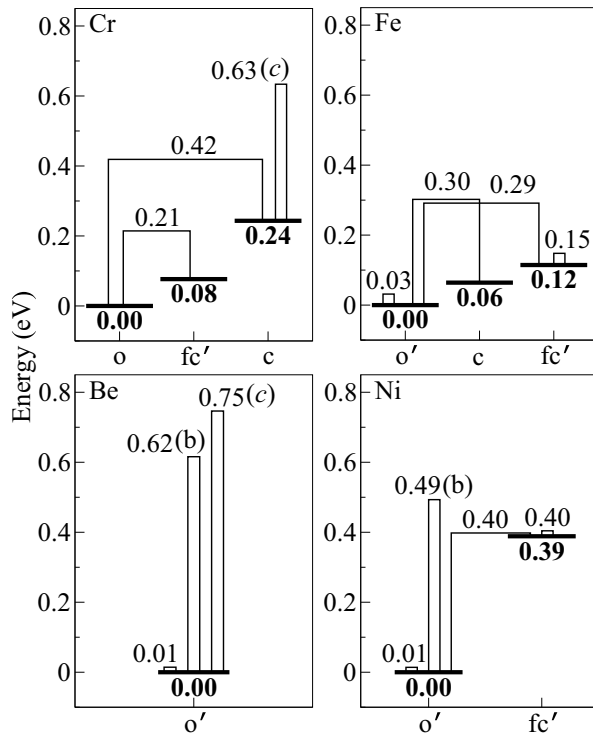


FIG. 6. Relative energies of the stable interstitial sites and the transition states for Cr, Fe, Be, and Ni in Zr. The thick bold lines indicate the relative energy levels of the interstitial sites which are labeled below with the corresponding energy values. The thin lines starting from and ending at a site represent transitions between these sites. The values associated with these thin lines are the corresponding transition-state energies. We mark the diffusive transitions between same type of sites as (b) for a basal jump and (c) for a c -axis jump.

The diffusivity is nearly isotropic for all solutes except Sn, which diffuses slightly faster in the basal plane than along the c axis. As there is limited experimental data available for comparison, it is difficult to comment on the disagreement between theory and experiments. Analysis of the finite-size effects of the simulations, presented in Appendix A 2, shows that this is insufficient to explain this discrepancy; we found larger cells increase in the activation barrier, which in turn will cause larger disagreements with the experiments. Possible explanations for the disagreement could be faster diffusion in polycrystalline samples or a nonequilibrium vacancy concentration. The vacancy-mediated diffusion coefficients of Cr, Fe, Be, and Ni are 10^5 to 10^8 orders lower than the experimental data (not shown), which reinforces the idea that these solute diffuse via the interstitial mechanism at equilibrium.

Table II shows that the activation barriers and prefactors from Arrhenius fits of diffusion coefficients computed using the thirteen-frequency models agree well with the GF approach, while those from the eight-frequency model show large deviations for all solutes except for Al. For the eight- and thirteen-frequency models, we assume that the basal transitions are between lattice sites only and use the larger of two transition-state energies. Even with these approximations, the thirteen-frequency model predicts activation barriers within 20 meV of GF method for both basal and c -axis diffusion

of all solutes. We attribute these results to the fact that the unique transition state energies in the GF approach beyond the scope of thirteen-frequency model are comparable to the bulk transition state energies, as evident from LIMB comparisons presented in Appendix A 1. Therefore, the impact on diffusivity predictions are negligible. However, we see significant deviations between the eight-frequency and GF results. The crucial difference between eight- and thirteen-frequency models are the escape jumps out of the 1p and 1b configurations. The thirteen-frequency model assumes two unique escape jumps (basal and pyramidal) each from 1b and 1p sites, while the eight-frequency model assumes one unique escape jump each from 1b and 1p. We choose the escape rates which take the vacancy farthest away from the solute. For the eight-frequency model, these rates correspond to the 1b-6b and 1p-5p jumps. For the thirteen-frequency model, these jumps are 1b-6b, 1b-4p, 1p-4p, and 1p-5p. The latter combination creates an energy landscape which closely approximates the transition pathways when considering the full range of interactions. However, the limited choices in the eight-frequency model severely restrict the diffusion pathways, causing deviations in the activation barrier predictions.

Figure 8 shows that the basal and c -axis drag ratios of Cr, Fe, Be, and Ni are positive while those of Sn and Al are negative, and there is good agreement between the GF and KMC results. Similar to the diffusion coefficients, we compute the results for Al and Ni using only the GF method. A positive drag ratio depends on two factors: (1) attractive binding energies and (2) low migration barriers for the vacancy to reorient around the solute compared to dissociation barriers, which increases the probability that the solute and vacancy diffuse as a complex. We attribute the negative drag ratios of Sn and Al to the repulsive binding energies, which cause vacancies to form away from the solute. The reorientation jump barriers for Sn and Al are comparable to the dissociation jump barriers and do not contribute to drag. For Cr, Fe, Be, and Ni, even though most of the binding energies are repulsive, a crucial difference is the low transition-state energies of jumps in the farther neighbor shells. As a result, if the vacancy migrates toward the solute atom, it undergoes repeated transitions within the thermodynamic range of solute. Therefore, the solute and vacancy diffuse as a complex instead of the vacancy escaping away from the thermodynamic range. For example, a common factor for these four solutes is the low barrier to jump from 1b to 1b1b: 0.250 eV for Cr, 0.115 eV for Fe, 0.129 eV for Be, and 0.116 eV for Ni. These barriers are much smaller than the escape barriers, which are close to 0.5 eV. Therefore, Cr, Fe, Be, and Ni can exhibit drag via vacancy fluxes in the HCP Zr matrix.

Figure 9 shows that the drag ratios change significantly depending on the model used to approximate the energy landscape, even though the changes in diffusion coefficients may be negligible. We find that replacing the double-humped barrier with a single transition that uses the maximum transition-state energy closely approximates the results with all states included. The largest changes are for the basal drag ratios of Sn, with differences between 0.18 to 0.25 for 600 K to 1235 K. Substituting the metastable state energy for transition states results in increased deviations, most notable for Sn, Be, and

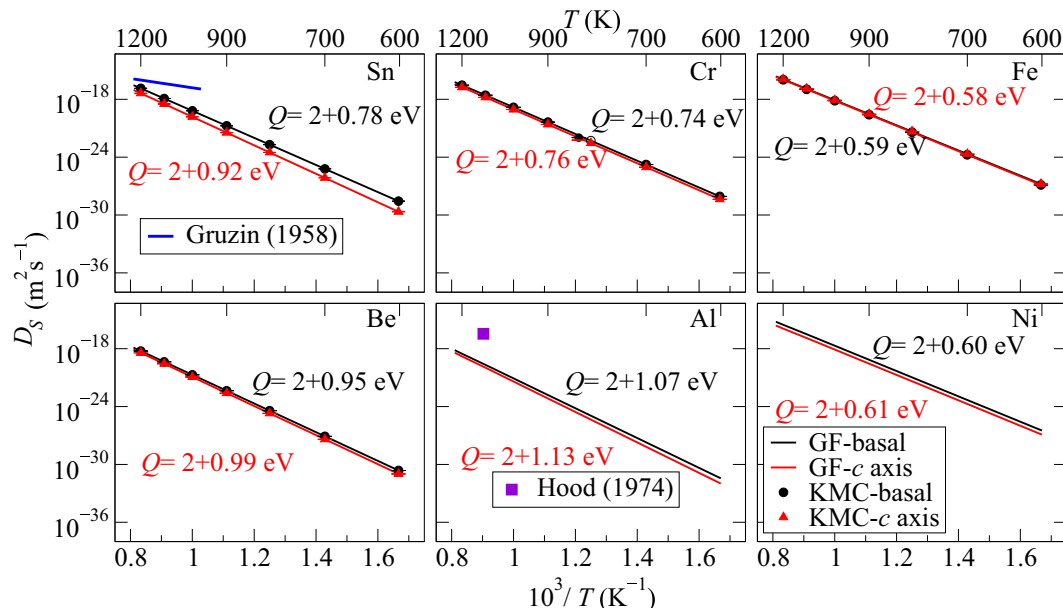


FIG. 7. Diffusion coefficients and activation barriers for vacancy-mediated transport of the solutes Sn, Cr, Fe, Be, Al, and Ni in Zr along the basal plane (black) and parallel to the c axis (red). We show the activation barriers as sum of two values, where the first value is the contribution from the vacancy-formation energy and the second value includes contributions from the binding energy and the dominant migration barriers in the diffusion calculations. For Sn, Cr, Fe, and Be, we compare the diffusivities computed using GF and KMC, and the results are in good agreement. We also plot the available experimental data for Sn [45] and Al [74]. The diffusivity is nearly isotropic for all solutes except Sn.

Al. In particular, the c -axis drag ratio of Be becomes negative above 1200 K, thus predicting a crossover temperature. The largest observable change is in the basal drag ratio of Al with differences between 1.23 to 0.16 from 600 K to 1235 K. However, there is no qualitative change in the drag behavior of Al as the values remain negative throughout the temperature range. The eight- and thirteen-frequency models, on the other hand, lead to both qualitative and quantitative changes in drag predictions for some of the solutes. For example, the thirteen-frequency model predicts a crossover temperature for basal drag of Sn at 700 K, c -axis drag of Cr at 1120 K, c -axis drag of Be at 990 K, and basal drag of Al at 1170 K. Similarly, the eight-frequency model predicts a crossover temperature for c -axis drag of Cr at 1100 K, c -axis drag of Be at 1080 K, and basal drag of Al at 1060 K. We expect these results to change if different combinations of escape rates are used in the eight- and thirteen-frequency models. In addition, these models also treat the two different transitions between 1b sites as equivalent (1b-1b1b and 1b-1b1b). A recent study [15] discusses how this approximation influences drag ratios, depending on the relative magnitudes of 1b-1p, 1p-1p, 1b-1b, and 1b-1b migration barriers. None of the approximations have a significant impact on the drag behavior of Fe and Ni—which suggests that even the transition rates accounted for by eight-frequency model are sufficient to capture the correlation between solute and vacancy fluxes. Based on these results, we conclude that accurate prediction of drag ratios potentially requires treating all symmetry unique states and transitions up to the sixth neighbor shell. Replacing the double-humped barrier with a direct transition using the larger energy is a reasonable approximation for predicting drag. However, it is worth pointing out that efficiently obtaining the correct DFT transition state energy for any basal jump first involves

relaxing the metastable state, followed by single-image CNEB calculations between the metastable configurations and the lattice sites. At the very least, computing the metastable state energy is useful because the migration barriers may be approximated using LIMB. As demonstrated in Appendix A 1, linear interpolation works better between a lattice site and the metastable state.

Figure 10 shows that the calculated interstitial solute diffusion coefficients for Cr, Be, and Ni agree with the experimental measurements within one order of magnitude, while

TABLE II. Activation barriers (E^a) and prefactors (ν) from Arrhenius fits of vacancy-mediated diffusion coefficients ($D = \nu e^{-E^a/k_B T}$). The barriers are in eV and the prefactors are $10^{-6} \text{ m}^2/\text{s}$. The activation barrier predictions from full treatment and the thirteen-frequency model are within 20 meV. The eight-frequency model shows larger deviations for all solutes except Al.

Solute	direction	Full		13 frequency		8 frequency	
		ν	E^a	ν	E^a	ν	E^a
Sn	Basal	0.531	2.784	0.603	2.792	0.607	2.922
	c axis	0.633	2.924	0.704	2.933	0.707	3.065
Cr	Basal	0.770	2.744	0.859	2.754	0.866	2.830
	c axis	0.567	2.764	0.625	2.772	0.625	2.824
Fe	Basal	1.318	2.596	1.554	2.606	1.430	2.764
	c axis	0.638	2.582	0.729	2.591	0.729	2.711
Be	Basal	0.106	2.948	0.113	2.955	0.113	2.994
	c axis	0.100	2.986	0.107	2.994	0.107	3.037
Al	Basal	0.186	3.070	0.202	3.067	0.202	3.067
	c axis	0.187	3.134	0.202	3.131	0.202	3.131
Ni	Basal	2.048	2.604	1.997	2.603	1.987	2.806
	c axis	0.886	2.611	0.867	2.609	0.867	2.785

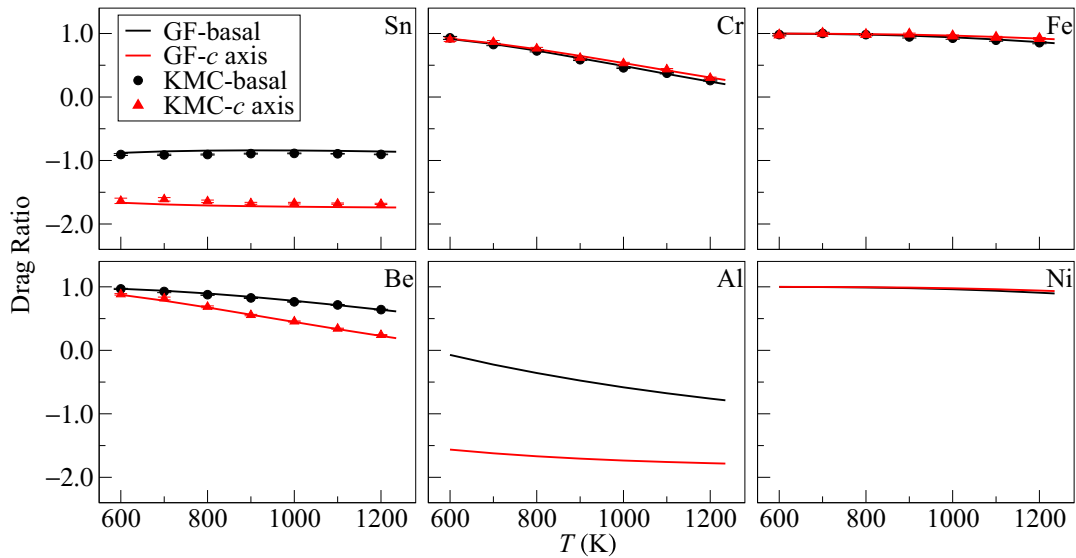


FIG. 8. The drag ratios L_{SV}/L_{SS} in the basal plane and parallel to the c axis. The drag ratios computed using the Green’s function method (GF) and kinetic Monte Carlo (KMC) are in good agreement for Sn, Cr, Fe, and Be. The drag ratios for Sn and Al remain negative throughout, while for Cr, Fe, Be, and Ni they are positive. For Ni and Fe, the drag ratios in both the basal plane and parallel to the c axis are close to one.

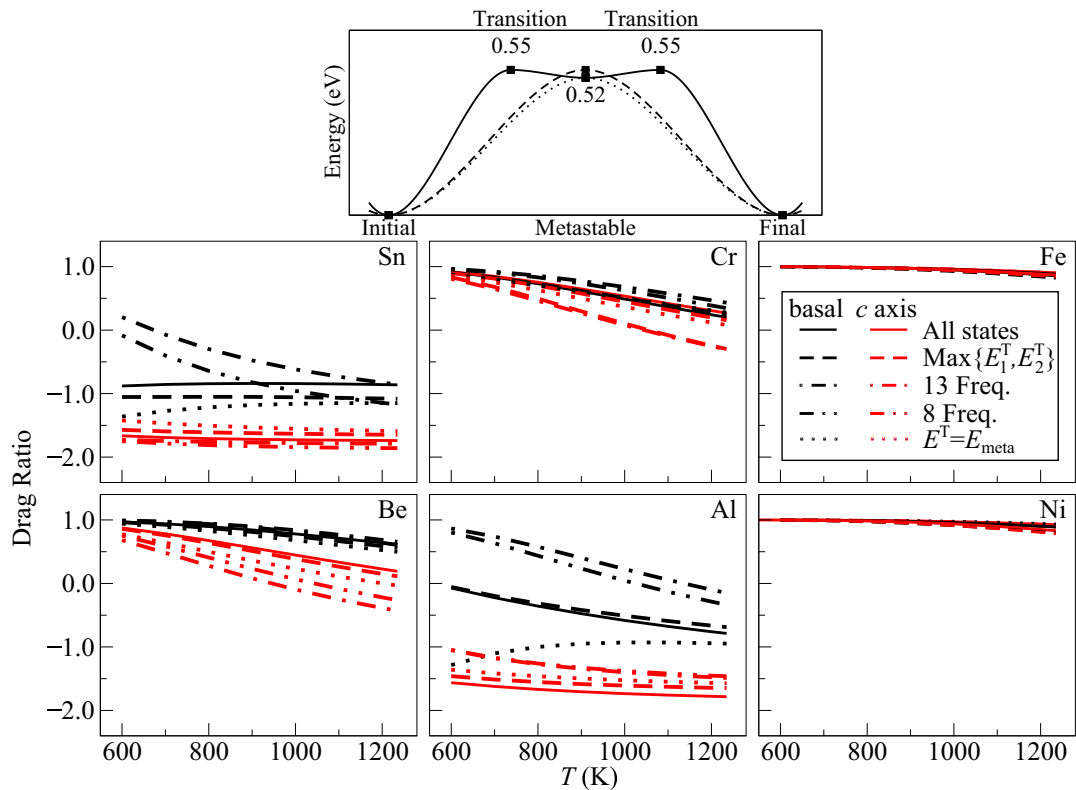


FIG. 9. Comparison of drag ratios computed with full treatment (All states) to those computed with metastable states omitted, the thirteen-frequency model, and the eight-frequency model. We use two different treatments for basal transitions when omitting metastable states: the vacancy transitions directly between lattice sites with the largest migration barrier ($E^T = \text{Max}\{E_1^T, E_2^T\}$), and metastable state is the transition state ($E^T = E_{\text{meta}}$). Top figure illustrates the two different treatments and compares them with the full treatment of metastable states for the case of basal vacancy migration in Zr. The drag ratios computed by omitting metastable states deviate from the results of the full treatment, with largest changes for Sn and Al. The drag ratios computed from both eight- and thirteen-frequency models show large changes for Sn, Cr, Be, and Al. The differences between the results from different treatments are negligible for Fe and Ni.

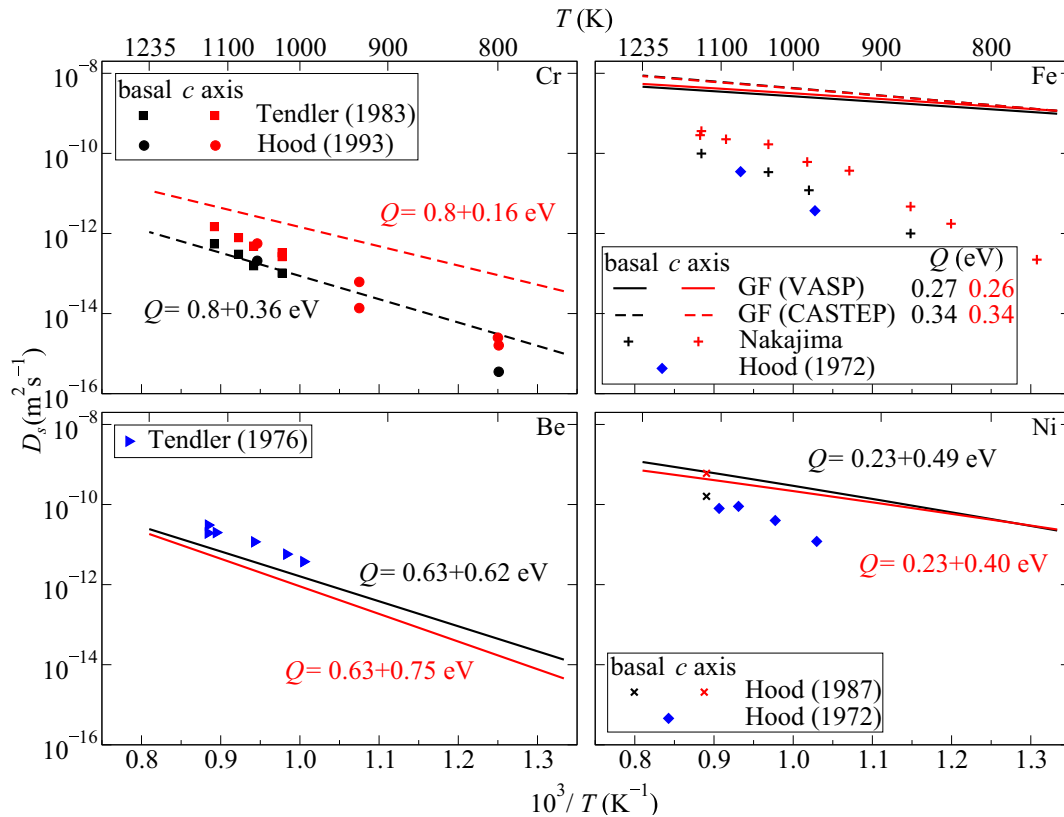


FIG. 10. The calculated interstitial diffusivities compared to the experimental data for the solutes Cr [40,41], Fe [42,43], Be [75], and Ni [43,44] in Zr. The basal and c -axis diffusivities and the corresponding activation barriers (Q) are in black and red, respectively. The experimental diffusivities from polycrystalline samples are in blue. We write the activation barriers for Cr, Be, and Ni as sum of two values; the first value is the energy of the ground-state interstitial site relative to the substitutional site; the second value corresponds to the dominant migration barrier; we skip this notation for Fe because the interstitial sites are lower in energy. The diffusivities for Cr, Be, and Ni agree well with the experimental data. The VASP and CASTEP calculations for Fe are in good agreement but the calculated diffusion coefficients are two orders of magnitude higher than the experimental data.

those of Fe are within two orders of magnitude. We correctly predict the anisotropy of diffusion for Cr. For Fe, we also present the results obtained by repeating the calculations using a larger cell (150 atoms) and a different DFT code (CASTEP) (see Appendix A 2 for details), showing good agreement, which indicates negligible effects due to differences in DFT codes, pseudopotentials, and supercell sizes. However, the calculations predict nearly isotropic diffusivities for Fe, while experimental results show faster diffusion along the c axis. These disagreements between theoretical calculations and experimental measurements suggest that the simplistic mechanism of a single solute atom jumping through the interstitial network does not accurately describe the diffusion of Fe in Zr, even for dilute concentrations. Moreover, the experimental results show two distinct slopes above and below 900 K, which suggests different processes maybe dominating. Burr *et al.* [51] used DFT calculations to demonstrate that Fe dumbbells in Zr have lower formation energies than isolated point defects, and that even dilute concentrations of Fe could exhibit clustering tendencies. However, more work is necessary to determine the effect of Fe dumbbells and clusters on the transport mechanisms. To our knowledge, there are no single crystal diffusivity measurements for Be diffusion in Zr.

For Ni, we found single-crystal diffusivity measurements at one temperature only [44]. Therefore, it is difficult to make valid comparisons with experiments regarding the diffusion anisotropy of Be and Ni in Zr. Lastly, we expect the values of the activation barriers to be similar to the dominant migration barriers. However, we note that only Be and Ni show this behavior but the activation barriers for Cr and Fe are smaller than the dominant migration barriers. The reason for this anomaly is that at high temperatures, the probability of occupying the higher energy sites for these solutes is comparable to that of the ground state, because the site energy differences are similar to $k_B T$. As a result, the average energy of the interstitial site is higher than the ground-state energy, and consequently, the activation barriers are smaller than the dominant migration barriers.

V. VACANCY SUPERSATURATION

At thermal equilibrium, both vacancy-mediated and interstitial mechanisms contribute to the total diffusivity D_S of the solute S . The total diffusivity D_S is then a weighted sum of the interstitial diffusion coefficient D_{S_i} and the vacancy-mediated

diffusion coefficient $D_{S_{Zr}}$

$$D_S = f_{S_i} D_{S_i} + f_{S_{Zr}} D_{S_{Zr}}. \quad (19)$$

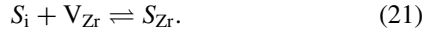
Note that vacancy-mediated diffusion requires the vacancies to exchange with the solute atoms; therefore, the term $D_{S_{Zr}}$ is proportional to the vacancy concentration c_V . The terms f_{S_i} and $f_{S_{Zr}}$ are the fractional concentrations of the solute as interstitial and substitutional defects

$$f_{S_i} = \frac{c_{S_i}}{c_{S_i} + c_{S_{Zr}}} = \frac{c_{S_i}}{c_S}, \quad (20)$$

$$f_{S_{Zr}} = \frac{c_{S_{Zr}}}{c_{S_i} + c_{S_{Zr}}} = \frac{c_{S_{Zr}}}{c_S},$$

where c_{S_i} is the interstitial solute concentration and $c_{S_{Zr}}$ is the substitutional solute concentration.

The solute atoms occupying the interstitial sites combine with the vacancies to form substitutional solutes via the Frank-Turnbull [76] mechanism. As a result, the concentration of solute at interstitial and substitutional sites can be affected by vacancies through the reaction



If the solutes and vacancies are in local equilibrium through this reaction, then we can apply the law of mass action to find

$$a_{S_i} a_V = k a_{S_{Zr}} \quad (22)$$

for a temperature-dependent reaction constant k and activities a_{S_i} , $a_{S_{Zr}}$, and a_V of the interstitial solute, substitutional solute, and vacancy. For dilute solute and vacancy concentrations, we can rewrite Eq. (22) in terms of concentrations of the interstitial solute c_{S_i} , vacancy c_V , and substitutional solute $c_{S_{Zr}}$

$$c_{S_i} c_V = \frac{c_{S_i}^{eq} c_V^{eq}}{c_{S_{Zr}}^{eq}} c_{S_{Zr}}, \quad (23)$$

where c_V^{eq} , $c_{S_i}^{eq}$, and $c_{S_{Zr}}^{eq}$ are the equilibrium vacancy, interstitial, and substitutional solute concentrations. Rearranging Eq. (23) using Eq. (20) gives

$$\frac{f_{S_i}}{f_{S_{Zr}}} = \frac{c_V^{eq}}{c_V} \left(\frac{f_{S_i}^{eq}}{f_{S_{Zr}}^{eq}} \right), \quad (24)$$

where the term in parentheses depends only on temperature. We plot the fractional concentrations in Fig. 11 for the four solutes at equilibrium, which shows that Cr and Be prefer substitutional sites and Fe prefers interstitial sites at equilibrium throughout the temperature range. Nickel starts out at substitutional sites but there is an appreciable increase in interstitial fraction at higher temperatures.

Radiation damage or quenching leads to supersaturated vacancy and self-interstitial concentrations in the Zr matrix, as evidenced by the formation of $\langle a \rangle$ and $\langle c \rangle$ loops in irradiated Zr samples [54–57]. The $\langle a \rangle$ loops develop at lower fluences and are formed by both interstitials and vacancies, while the $\langle c \rangle$ loops develop at higher fluences and are formed by vacancies only. Moreover, interstitials diffuse much faster than the vacancies for a range of temperatures and annihilate at sinks while the vacancies accumulate. Therefore, we expect higher vacancy concentrations at longer lifetimes of zirconium alloys. A nonequilibrium vacancy concentration retained in the matrix can change the equilibrium between the interstitial

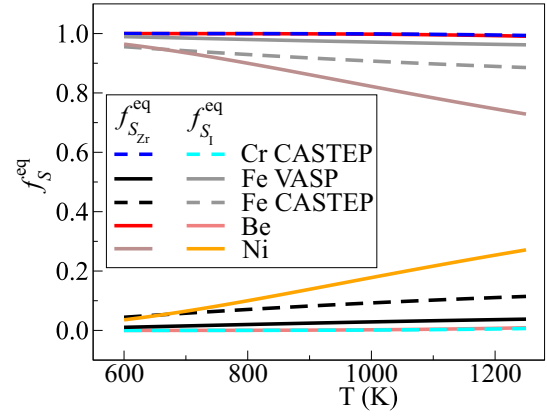


FIG. 11. The fractional substitutional and interstitial solute concentration of Cr, Fe, Be, and Ni at equilibrium as a function of temperature. Solid lines correspond to data from VASP calculations and dotted lines correspond to data from CASTEP calculations.

solutes and substitutional solutes by decreasing the fraction of interstitials. If the vacancy concentration remains dilute, then the fractional solute concentrations under nonequilibrium vacancy concentrations

$$f_{S_i} = \frac{f_{S_i}^{eq} c_V^{eq}}{f_{S_{Zr}}^{eq} c_V + f_{S_i}^{eq} c_V^{eq}},$$

$$f_{S_{Zr}} = \frac{f_{S_{Zr}}^{eq} c_V}{f_{S_{Zr}}^{eq} c_V + f_{S_i}^{eq} c_V^{eq}}. \quad (25)$$

The contribution from interstitial diffusion $f_{S_i} D_{S_i}$ scales with c_V^{-1} , while the contribution from vacancy-mediated diffusion $f_{S_{Zr}} D_{S_{Zr}}$ scales with c_V . Therefore, excess vacancies modify the contributions from different diffusion mechanisms and a sufficiently high vacancy concentration may cause the vacancy-mediated diffusion mechanism to dominate even if the interstitial diffusion mechanism dominates at equilibrium.

Figure 12 shows nonmonotonic behavior of diffusion with increasing vacancy concentration connected to changes in the dominant diffusion mechanism. The excess vacancies decrease the concentration of solute at interstitial sites while increasing the substitutional sites. As a result, the contribution from interstitial diffusion decreases while the contribution from vacancy-mediated diffusion increases. Since the interstitial mechanism dominates at equilibrium, the diffusion decreases until both mechanisms contribute equally. Further increases in vacancy concentration causes the vacancy-mediated mechanism to dominate and the diffusion coefficient increases. The slowdown in interstitial diffusion due to excess vacancies may provide an alternate explanation for the discrepancy between theoretical predictions and experimental measurements for Fe diffusion in Zr, as high vacancy concentration would contribute to slower diffusion.

VI. CONCLUSION

We extend a recently developed Green's function methodology to accurately model the vacancy metastable states observed in Zr and calculate transport coefficients for vacancy-mediated diffusion and interstitial in the dilute limit

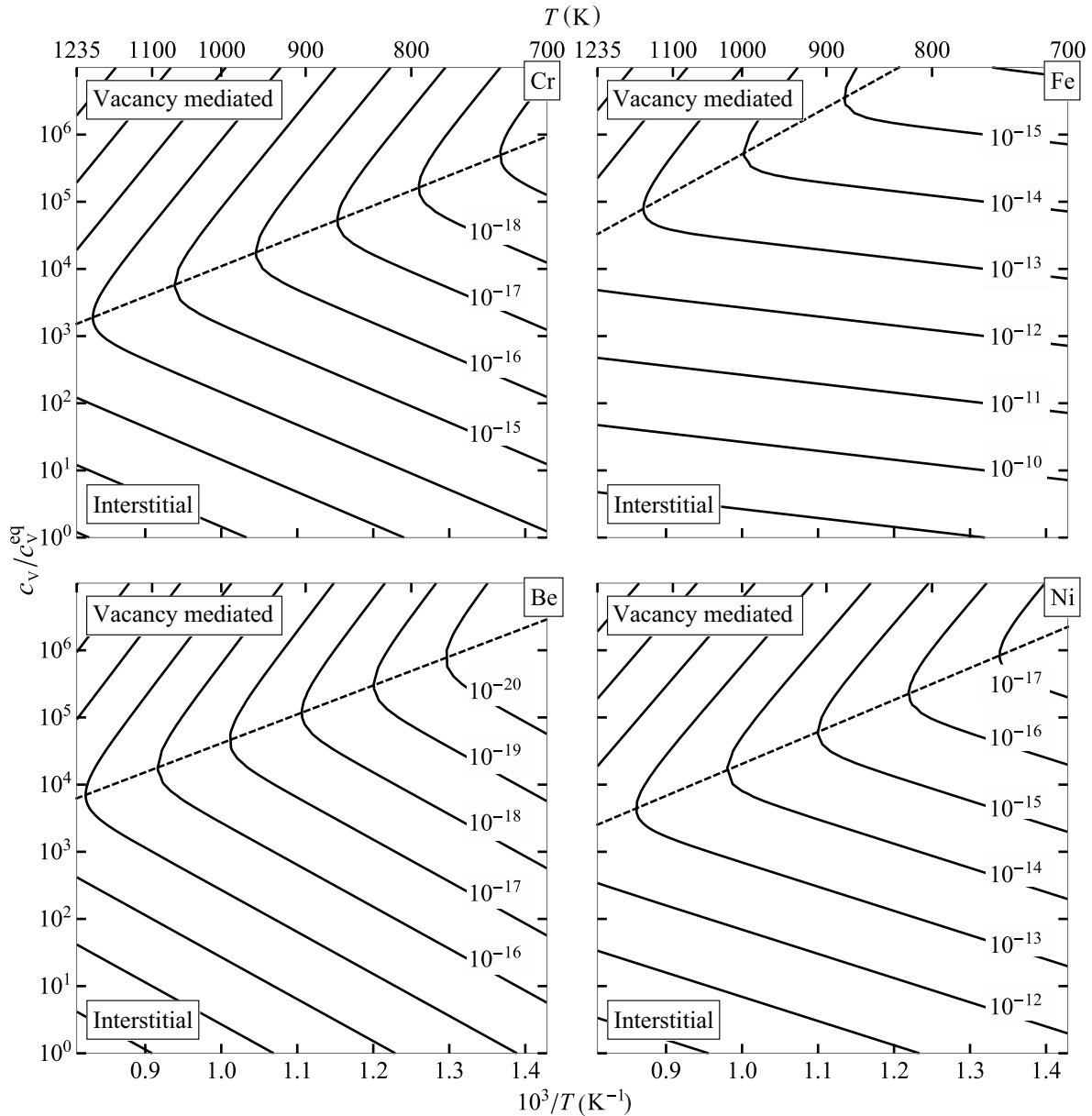


FIG. 12. Diffusivity of Cr, Fe, Be, and Ni in m^2/s as a function of temperature and the ratio c_v/c_v^{eq} of supersaturated vacancy concentration to equilibrium vacancy concentration. The dashed line separates the upper region where the vacancy-mediated mechanism dominates from the lower region where the interstitial mechanism dominates. The diffusion coefficients are the sum of interstitial diffusion and vacancy-mediated diffusion mechanisms as a function of c_v/c_v^{eq} , using Eqs. (19) and (25).

of the solutes Sn, Cr, Fe, Be, Al, and Zr in the HCP Zr matrix. We perform DFT calculations to determine the set of unique solute-vacancy complexes and transition rates in Zr which inform both the GF methodology and the KMC simulations. The excellent agreement between the calculated diffusivities and the experimental measurements validates our methodology and results. The calculated drag ratios for Cr, Fe, Be, and Ni are positive, which suggests that vacancy fluxes at nonequilibrium concentrations can drag these solutes toward sinks such as grain boundaries, dislocation loops, and surfaces. We also compute the transport coefficients using eight- and thirteen-frequency models, and our results indicate that accurate treatment of energies and transition rates up to the sixth neighbor shell is essential to correctly predict the

drag ratios for solutes such as Sn, Cr, Be, and Al. The transport coefficients calculated in this work can inform higher length-scale models which study microstructural changes such as solute segregation, growth of precipitates, etc.

For the first time, we demonstrate the effect of irradiation on the atomic scale diffusion mechanisms by combining the interstitial diffusivities computed in this study and the vacancy-mediated diffusivities. We predict that a nonequilibrium vacancy concentration can slow down interstitial diffusion and accelerate vacancy-mediated diffusion and that a sufficiently high radiation-induced vacancy concentration could change the dominant diffusion mechanism. The combined results of interstitial and vacancy-mediated diffusion can also inform higher length-scale models, which allow for the

modeling of solute redistribution behavior under irradiation. The change in transport mechanisms at higher vacancy concentrations reinforces the importance of performing atomic-scale transport studies, as experimental diffusivity measurements carried out at equilibrium are insufficient to account for the effects of irradiation.

The excess vacancies not only affect the transport mechanisms in systems under irradiation but also have consequences for diffusion in any system containing nonequilibrium point defect concentration. We demonstrate that the excess vacancies strongly influence transport if the solute prefers substitutional sites. For such solutes, it is imperative to maintain a near-equilibrium vacancy concentration during diffusion experiments; otherwise, the measurements will overpredict diffusivity if the vacancy-mediated mechanism dominates or underpredict diffusivity if the interstitial mechanism dominates. Moreover, even the excess vacancies retained during quenching can significantly influence diffusion, particularly in metals with low vacancy-formation energies.

All of the computational data are available in a publicly accessible database [77].

ACKNOWLEDGMENTS

This research was supported by the U.S. Department of Energy NEUP Project No. IRP-12-4728. The computational resources were provided by the University of Illinois Campus Cluster and the National Energy Research Scientific Computing Center, the Australian National Computational Infrastructure (NCI), and the Multimodal Australian Sciences Imaging and Visualisation Environment (MASSIVE). The geometry figures were drawn using the JMOL package [78].

APPENDIX A: DENSITY-FUNCTIONAL THEORY COMPARISONS

1. LIMB predictions of transition state energies

Figure 13 shows poor agreement between LIMB predictions using Eq. (17) and NEB calculations of the pyramidal transition-state energies for the vacancy jumps closer to the solute, but the agreement improves for jumps which are fur-

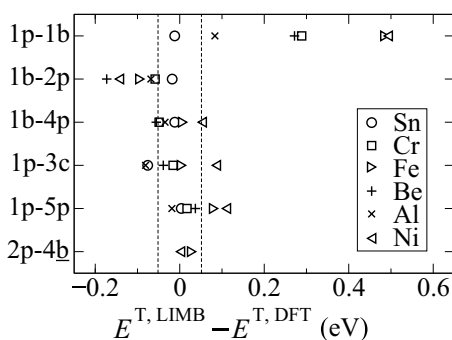


FIG. 13. Difference between the transition-state energies from LIMB predictions using Eq. (17) and NEB calculations of pyramidal vacancy jumps. The dotted lines correspond to $\pm k_B T$ at $T = 600$ K. The LIMB predictions disagree with NEB for the jumps 1p-1b and 1b-2p, but the agreement improves for the jumps to farther neighbors.

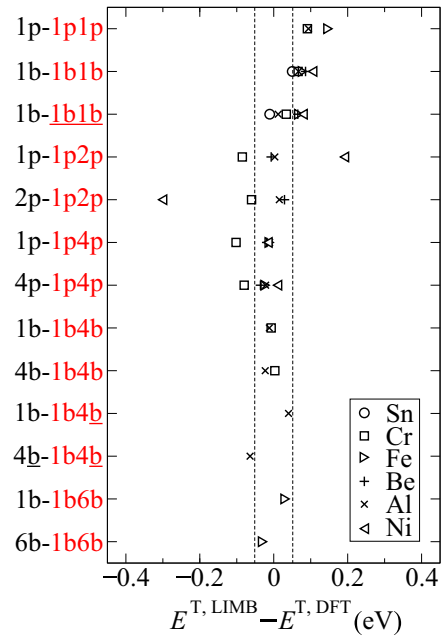


FIG. 14. Differences between the transition-state energies from LIMB predictions using Eq. (18) and NEB calculations for basal vacancy jumps. The dotted lines correspond to $\pm k_B T$ at $T = 600$ K. The LIMB predictions are generally in good agreement with NEB except for the jumps between first nearest neighbors, and a few outliers such as the jumps out of 1p2p for Ni. The latter case can be attributed to the low binding energy of Ni with vacancy at the 1p2p metastable state.

ther out. Since we are interested in temperatures above 600 K, we set our error tolerance to $\pm k_B T$ at $T = 600$ K, marked by the dotted lines on the figure. For Sn, LIMB agrees well with DFT for all the jumps. In cases of Cr, Be, and Al, LIMB disagrees with DFT for 1p-1b and 1b-2p but the difference is within tolerance for further jumps. In cases of Fe and Ni, LIMB disagrees with DFT for almost all jumps out of 1b and 1p but agrees within tolerance for the 2p-4b jump. We use DFT energies for the transitions shown in Fig. 13 but use LIMB to approximate the further transitions such as 4p-4b, 2p-5p, 4p-5p, etc. We use the attempt frequencies of the bulk pyramidal jump for the interpolated transitions in the LIMB approximation.

Figure 14 shows an overall good agreement between LIMB predictions using Eq. (18) and NEB calculations of the transition-state energies for basal jumps between lattice sites and metastable states. There are a few outliers such as jumps between the first nearest neighbors for all the solutes and the jumps out of 1p2p for Ni. For Sn, the two jumps out of 1b show good agreement and the rest of the metastable states connecting 1b and 1p to the next nearest neighbors are unstable. For Cr, LIMB disagrees with DFT for the jumps out of 1p1p, 1b1b, 1p2p, and 1p4p, but the agreement improves for 1b4b. Beyond 1p1p, 1b1b, and 1b1b, the agreement is good for Fe, Be, and Al. For Ni, the disagreement for jumps out of 1p2p is high and we attribute this to the large attractive binding energy of the 1p2p complex and its unusual geometry where the moving Zr atom displaces close to the solute. Similar to

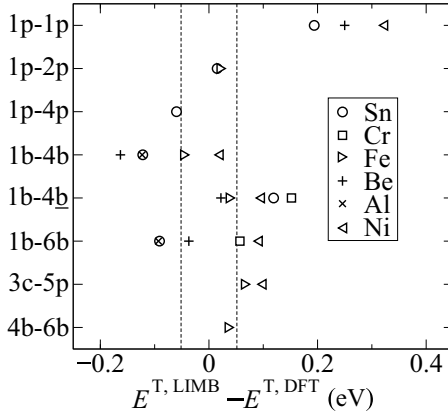


FIG. 15. Difference between the transition-state energies from LIMB predictions using Eq. (17) and NEB calculations of basal jumps where there are no metastable states. The dotted lines correspond to $\pm k_B T$ at $T = 600$ K. For such jumps, LIMB predictions generally disagree with NEB and we use the NEB energies as input to our diffusion model.

the case of pyramidal jumps, we use DFT energies for the transitions shown in Fig. 14 but use LIMB to approximate further basal transitions such as 2p-2p4p, 4p-2p4p, 4p-4p4p, etc. We use the attempt frequencies of the bulk basal jump for the interpolated transitions.

Figure 15 shows that LIMB predictions using Eq. (17) and NEB calculations generally disagree for the transition-state energies of basal jumps where metastable states are unstable. Such cases have no bulk analog, so we use Eq. (17) to estimate the transition-state energies by making the following choices: (1) We set $r = 0.5$ (where the transition state would be if the bulk metastable state was unstable), and (2) we use the energy of the basal transition state $E_{0i_V-0i_V j_V}^{T, DFT}(V, Zr_{M-1})$ for $E_{0i_V-x'_{i_V} i'_V}^{T, DFT}(V, Zr_{M-1})$. However, our choice of linear interpolation is insufficient to capture the changes induced by solutes to the energy landscape, and most of the LIMB predictions differ from NEB by more than the error threshold of $\pm k_B T$ at $T = 600$ K. Therefore, we use NEB to compute the transition state energies of all jumps where there are no metastable states and use the computed values in our diffusion calculations.

TABLE III. Comparison of vacancy formation energies and migration barriers computed from VASP and CASTEP. The values of the migration barriers are relative to the ground-state vacancy configuration. The change in the vacancy formation energies and the basal vacancy jump barrier are less than 25 meV while the change in the pyramidal jump barrier is 68 meV between the 96-atom and 288-atom CASTEP calculations.

	VASP-96	CASTEP-96	CASTEP-150	CASTEP-288
Formation energy (eV)				
Ground state	2.002	2.048	2.061	2.025
Metastable state	2.517	2.609		2.597
Migration barrier (eV)				
Basal	0.553	0.598	0.591	0.609
Pyramidal	0.631	0.682	0.729	0.750

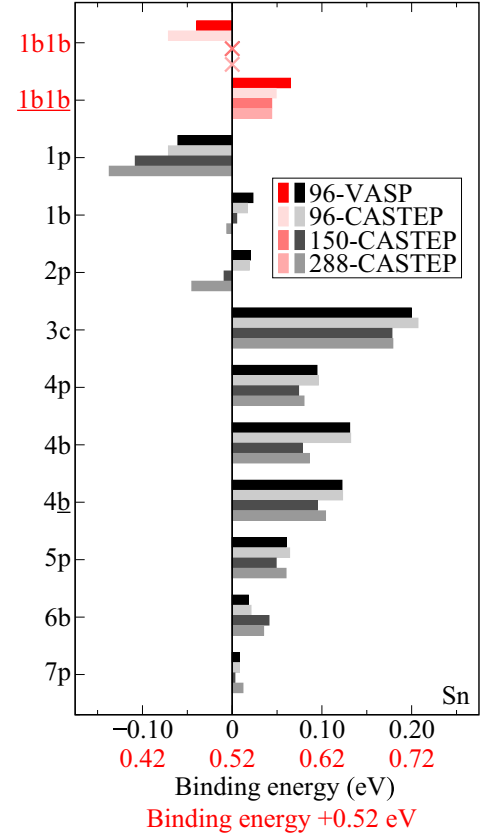


FIG. 16. Comparison of binding energies for Sn-vacancy complexes using different DFT codes and supercell sizes. The gray shaded bars and the black horizontal scale measure the binding energies of lattice sites, while the red shaded bars and the red scale are for metastable states. We shift the red scale by 0.52 eV, which is the energy of vacancy in bulk metastable configuration relative to the ground-state configuration of the 96-atom VASP calculation. The results of the 96-atom supercell calculations from VASP and CASTEP are in good agreement. The intermediate state 1b1b is unstable in the 150-atom and 288-atoms CASTEP calculations. The 1p and 2p sites show the largest differences in the binding energies across supercell sizes: 65 and 62 meV, respectively. The rest of the changes are less than 25 meV.

2. Finite-size effects in the DFT calculations

We investigate the variability of results with different DFT codes, pseudopotentials, and supercell sizes by performing calculations of Sn in Zr with the CASTEP code [79]. We choose Sn for this parallel study for several reasons: We can eliminate the effect of magnetism from our study; albeit limited, there is some experimental data for Sn; and lastly, we expect Sn to diffuse via the vacancy-mediated mechanism and serve as validation for our methodology. We use the PBE functionals with ultrasoft pseudopotentials [80] and a plane-wave energy cutoff of 450 eV. We describe the Zr and Sn atoms with $[Ar 3d^{10} 4s^2 4p^6 4d^2 5s^2]$ and $[Kr] 4d^{10} 5s^2 5p^2$ valence electrons. We kept all other simulation parameters the same as those reported in Ref. [51]. We use supercells containing 96, 150, and 288 Zr atoms ($4 \times 4 \times 3$, $5 \times 5 \times 3$, and $6 \times 6 \times 4$ replicas of the conventional unit cell). We keep the k -point density as constant as possible across the three supercells, using

TABLE IV. Comparison of vacancy migration barriers for Sn as a substitutional solute in Zr, computed from VASP and CASTEP. The values of the migration barriers are relative to the initial site. The complex 1b1b is unstable in the 150-atom and 288-atom CASTEP calculations and there is a direct 1b-1b transition. The basal and pyramidal exchange barriers show the largest changes between supercell sizes. The changes in the basal vacancy jump barriers are less than 25 meV while the 1p-1b pyramidal jump barrier changes by 39 meV between the 96-atom and 288-atom CASTEP calculations.

Jump	Migration barriers (eV)			
	VASP-96	CASTEP-96	CASTEP-150	CASTEP-288
Basal exchange	0.764	0.815	0.807	0.898
Pyramidal exchange	0.992	1.040	1.070	1.156
1p-1b	0.667	0.717	0.778	0.756
1b-1b1b	0.461	0.502		
1b-1b			0.507	0.516
1b-1b1b	0.593	0.655	0.671	0.645

Monkhorst-Pack [66] k -point meshes of $4 \times 4 \times 3$, $3 \times 3 \times 3$, and $2 \times 2 \times 2$ and a Methfessel-Paxton smearing width of 0.1 eV. Notably, we observe a significant difference in binding energies with coarser k -point grids. The convergence criterion for electronic minimization is an energy difference smaller than 10^{-8} eV. We relax the atomic configurations at constant volume with the memory-reduced BFGS algorithm [81,82] until forces on atoms are less than 10 meV/Å. We use the linear and quadratic synchronous transit method (LST/QST) [83] within CASTEP to determine the transition states for vacancy jumps. We did not enforce symmetry operations on any of the CASTEP calculations.

Table III shows that the 96-atom VASP calculations and the 96-, 150-, and 288-atom CASTEP calculations all predict similar vacancy formation energies and bulk vacancy migration barriers in Zr. Our findings suggest that the existence of a metastable state is independent of the DFT codes and

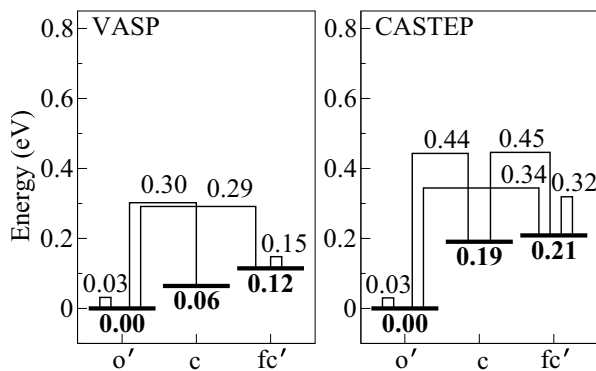


FIG. 17. Comparison of 96-atom VASP and 150-atom CASTEP calculations of site and transition state energies for interstitial Fe in Zr. Both calculations predict the same set of stable interstitial sites with o' as the ground state. The relative energies of sites c and fc' differ between the two calculations by 130 and 90 meV, respectively. The transition-state energy between two calculations for the basal diffusive barrier o' - c differs by 140 meV and the c -axis diffusive barrier o' - fc' differs by 30 meV.

TABLE V. Mapping between the mathematical description of a solute vacancy complex state described in the methodology section and the simplified labels illustrated in Fig. 2. There are two basis sites in the HCP unit cell, $\frac{a}{12}[04\bar{4}3]$ and $\frac{a}{12}[40\bar{4}9]$, and we assume that the solute occupies the first basis site. We list the multiplicity of each state, a representative vector which describes the state relative to the position of the solute in Miller Bravais notation, and the distance between the solute and the vacancy (or the solute and the moving Zr atom for metastable state). The full set of symmetry equivalent vectors can be obtained using point group operations to transform the representative vector. Note that the set of vectors changes when the solute occupies the second basis site, and the space group operations transform the first set of vectors into the second set.

Site	Multiplicity	Representative vector	Distance (Å)
1p1p	6	$\frac{a}{6}[11\bar{2}3]$	2.749
1b1b	3	$\frac{a}{6}[30\bar{3}0]$	2.801
1b1b	3	$\frac{a}{6}[03\bar{3}0]$	2.801
1p	6	$\frac{a}{6}[02\bar{2}3]$	3.189
1b	6	$\frac{a}{6}[22\bar{4}0]$	3.234
1p2p	12	$\frac{a}{6}[21\bar{3}3]$	3.576
1p4p	12	$\frac{a}{6}[13\bar{4}3]$	4.245
1b4b	6	$\frac{a}{6}[14\bar{5}0]$	4.278
1b4b	6	$\frac{a}{6}[41\bar{5}0]$	4.278
2p	6	$\frac{a}{6}[40\bar{4}3]$	4.542
2p4p	12	$\frac{a}{6}[32\bar{5}3]$	4.822
1b6b	6	$\frac{a}{6}[33\bar{9}0]$	4.851
3c	2	$\frac{a}{6}[0006]$	5.171
4p4p	6	$\frac{a}{6}[05\bar{5}3]$	5.336
3c5p	12	$\frac{a}{6}[11\bar{2}6]$	5.418
4p	12	$\frac{a}{6}[24\bar{6}3]$	5.576
4b	6	$\frac{a}{6}[06\bar{6}0]$	5.602
4b	6	$\frac{a}{6}[60\bar{6}0]$	5.602
2p7p	12	$\frac{a}{6}[43\bar{7}3]$	5.806
4b6b	6	$\frac{a}{6}[25\bar{7}0]$	5.831
4b6b	6	$\frac{a}{6}[52\bar{7}0]$	5.831
5p5p	6	$\frac{a}{6}[30\bar{3}6]$	5.881
5p5p	6	$\frac{a}{6}[03\bar{3}6]$	5.881
5p	12	$\frac{a}{6}[22\bar{4}6]$	6.099
4p7p	12	$\frac{a}{6}[35\bar{8}3]$	6.240
6b	6	$\frac{a}{6}[44\bar{8}0]$	6.468
7p	12	$\frac{a}{6}[46\bar{10}3]$	7.212

potentials and it is not an artifact of the finite-size effect. We attribute the energy differences between VASP and CASTEP 96-atom calculations to the Zr potential used for the latter case, where the valence shell includes 4s and 4p electrons as well. Subsequent changes in supercell size add only 25 meV to vacancy formation energy and 11 meV to the basal migration barrier, which suggests that finite size does not have a significant affect on these energies. However, there is an increase of 68 meV between the 96-atom and 288-atom CASTEP calculations in the pyramidal barrier, which suggests stronger influence of finite-size effects on the barriers.

Figure 16 shows that finite-size effect lowers the Sn-vacancy binding energies by less than 25 meV for most configurations and Table IV shows that finite-size effects increase the Sn-vacancy exchange barriers. Comparing the 96-atom supercell calculations from VASP and CASTEP, we find the largest changes in the configurations and transitions closest

to the solute atom. The energy of the 1b1b configuration is lower by 35 meV, while the basal and pyramidal exchange barriers are higher by 49 and 48 meV, respectively. We note similar changes in the energy of transition states for jumps around the solute atom and we attribute these changes to the use of potentials with more valence electrons in the CASTEP calculations. Finite size strongly affects the binding energies of 1p and 2p configurations, which show differences of 65 and 62 meV, respectively, between 96-atom and 288-atom cells. We also find a metastable state between the basal solute-vacancy exchange when simulated in the 288-atom cell with CASTEP, which could modify the basal diffusion coefficient. Going from a 96-atom to 150-atom cell, the cell size increases in the basal plane but not along the c axis, while going from 150 to 288 atoms, cell size increases in both directions. For most configurations, the energy differences are larger between 96-atom and 150-atom calculations compared to 150-atom and 288-atom calculations, suggesting a larger finite-size effect on configurations in the basal plane than along the c axis. Among the migration barriers, the basal and pyramidal exchange barriers show the largest changes in the 288-atom CASTEP calculation: 83 and 116 meV higher than the corresponding 96-atom CASTEP calculations. However, the changes are less significant going from 96-atom to 150-atom calculations, suggesting stronger finite-size effects along the c axis on exchange jumps. The high exchange barriers will directly effect the diffusivities of Sn in Zr by increasing the activation energy for diffusion. Further, we note that the exchange barriers in all cases are larger than the vacancy migration barriers around the solute atom, which indicates that the solute-vacancy exchange is the rate-limiting step for the diffusion of Sn. While we did not compute the full range of transition-state energies using the larger cell sizes, the negligible changes in the site energies away from the Sn atom suggests that the far jumps will not be affected by larger supercell sizes.

Figure 17 shows that the 96-atom VASP and 150-atom CASTEP calculations predict the same set of sites and dominant transitions for Fe interstitials in Zr, but the site and transition

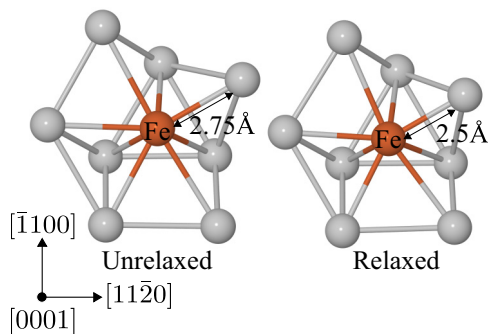


FIG. 18. The figure illustrates the unrelaxed and relaxed geometries of the 1b1b complex for the case of Fe in Zr. The neighbor cage compresses on relaxation in order to increase the nearest neighbors of Fe, which leads to stronger bonding. In particular, the distance between the Fe atom and the moving Zr atom located halfway between two 1b sites changes by 0.2 Å, while Fe displaces towards the $[0\bar{1}10]$ direction.

TABLE VI. Migration barriers ($E_{\alpha-\beta}^m$) and attempt frequencies ($\nu_{\alpha-\beta}$) for transitions. The barriers are in eV and the frequencies are in THz.

Solute	Jump	Forward		Reverse	
		$\nu_{\alpha-\beta}$	$E_{\alpha-\beta}^m$	$\nu_{\beta-\alpha}$	$E_{\beta-\alpha}^m$
Cr	o-fc'	8.087	0.214	3.207	0.137
	o-c	6.779	0.419	4.132	0.176
	c-c	5.945	0.390	5.945	0.390
Fe (VASP)	o'-o'	5.055	0.032	5.055	0.032
	o'-c	6.335	0.302	5.515	0.238
	o'-fc'	6.573	0.291	3.104	0.177
	fc'-fc'	2.968	0.034	2.968	0.034
Fe (CASTEP)	o'-o'	5.472	0.030	5.472	0.030
	o'-c	6.498	0.443	5.721	0.252
	o'-fc'	6.953	0.344	3.199	0.134
	c-fc'	6.104	0.255	3.189	0.236
Be	fc'-fc'	2.969	0.319	2.969	0.319
	o'-o'	13.095	0.014	13.095	0.014
	o'-o'(b)	13.217	0.615	13.217	0.615
Ni	o'-o'(c)	12.896	0.746	12.896	0.746
	o'-o'	4.950	0.014	4.950	0.014
	o'-o'(b)	5.931	0.493	5.931	0.493
	o'-fc'	4.485	0.399	2.757	0.009
	fc'-fc'	2.789	0.017	2.789	0.017

state energies are different. We extend the discussion presented in the first part of the study for Sn to Fe interstitials as well. Once again we can eliminate the effect of magnetism as interstitial configurations have a zero magnetic moment. Both calculations predict o' as the ground state, followed by c and fc'. We previously noted that using potentials with more electrons in the valence shell alone introduced energy differences of approximately 50 meV in the transition states. We attribute the additional differences to finite-size effects, such as the o'-c barrier computed from CASTEP, which is 140 meV higher. The CASTEP calculation predicts an additional diffusive jump c-fc'; however, it has a relatively high barrier of 260 meV which will not be dominant. Past DFT calculations of Fe in Zr using different codes and simulation parameters have shown significant variation in relative energies as well as ground states [28,51,52]. We find that the calculations performed

TABLE VII. Activation barriers (E^a) and prefactors (ν) from Arrhenius fits of diffusion coefficients ($D = \nu e^{-E^a/k_B T}$). The barriers are in eV and the prefactors are 10^{-6} m²/s.

Solute	Direction	VASP		CASTEP	
		ν	E^a	ν	E^a
Cr	Basal			0.072	1.16
	c axis			0.114	0.96
Fe	Basal	0.080	0.27	0.232	0.34
	c axis	0.058	0.26	0.221	0.34
Be	Basal	0.344	1.25		
	c axis	0.862	1.38		
Ni	Basal	0.566	0.72		
	c axis	0.140	0.63		

with lower k -point mesh size than $3 \times 3 \times 3$ for a $5 \times 5 \times 3$ cell size artificially stabilize Fe interstitial sites which are unstable, and even predict a nonmagnetic ground state for substitutional Fe which is higher in energy. Our results from two well-converged sets of calculations agree with each other; however, we expect the diffusion coefficients predicted using the CASTEP data set to have marginally higher activation barriers.

APPENDIX B: ADDITIONAL DATA

Table V contains the mapping representation of solute-vacancy complexes, Fig. 18 shows the relaxed geometry of the low-energy Fe solute-vacancy complex in Zr, Table VI contains the migration barriers and attempt frequencies for interstitial diffusion (cf., Fig. 6), while Table VII contains the Arrhenius fits for interstitial diffusion.

-
- [1] J. H. Schemel, *Zirconium in Nuclear Applications*, Vol. 551 of ASTM Special Technical Publication (American Society for Testing and Materials, Portland, Ore, 1974).
- [2] C. L. Whitmarsh, Review of Zircaloy-2 and Zircaloy-4 properties relevant to N.S. Savannah reactor design, Technical Report ORNL-3281 (Oak Ridge National Laboratory, Oak Ridge, TN (United States), 1962).
- [3] M. Griffiths, *J. Nucl. Mater.* **159**, 190 (1988).
- [4] B. Cox and H. Sheikh, *J. Nucl. Mater.* **249**, 17 (1997).
- [5] G. Sundell, M. Thuvander, and H.-O. André, *J. Nucl. Mater.* **456**, 409 (2015).
- [6] A. T. Motta, A. Couet, and R. J. Comstock, *Annu. Rev. Mater. Res.* **45**, 311 (2015).
- [7] A. Garner, J. Hu, A. Harte, P. Frankel, C. Grovenor, S. Lozano-Perez, and M. Preuss, *Acta Mater.* **99**, 259 (2015).
- [8] G. Sundell, M. Thuvander, and H.-O. André, *Corros. Sci.* **102**, 490 (2016).
- [9] Y. Dong, A. T. Motta, and E. A. Marquis, *J. Nucl. Mater.* **442**, 270 (2013).
- [10] B. de Gabory, Y. Dong, A. T. Motta, and E. A. Marquis, *J. Nucl. Mater.* **462**, 304 (2015).
- [11] A. Couet, A. T. Motta, and R. J. Comstock, in *Zirconium in the Nuclear Industry*, edited by B. Comstock and P. Barberis (ASTM International, West Conshohocken, PA, 2015), Vol. 17, pp. 479–514.
- [12] A. Chadwick and M. Terenzi, *Defects in Solids: Modern Techniques*, Nato Science Series B (Springer, New York, 2013).
- [13] D. R. Trinkle, *Philos. Mag.* **97**, 2514 (2017).
- [14] R. Agarwal and D. R. Trinkle, *Phys. Rev. B* **94**, 054106 (2016).
- [15] R. Agarwal and D. R. Trinkle, *Phys. Rev. Lett.* **118**, 105901 (2017).
- [16] R. Agarwal and D. R. Trinkle, *Acta Mater.* **150**, 339 (2018).
- [17] W. Zhong, P. A. Mouche, X. Han, B. J. Heuser, K. K. Mandapaka, and G. S. Was, *J. Nucl. Mater.* **470**, 327 (2016).
- [18] A. C. P. Jain and D. R. Trinkle, *Acta Mater.* **122**, 359 (2017).
- [19] C. Domain and A. Legris, *Philos. Mag.* **85**, 569 (2005).
- [20] D. H. Ruiz, L. M. Gribaudo, and A. M. Monti, *Mat. Res.* **8**, 431 (2005).
- [21] C. H. Woo and X. Liu, *Philos. Mag.* **87**, 2355 (2007).
- [22] G. V \acute{e} rit \acute{e} , F. Willaime, and C. C. Fu, *Solid State Phenom.* **129**, 75 (2007).
- [23] R. C. Pasianot and R. A. P \acute{e} rez, *Phys. B* **407**, 3298 (2012).
- [24] G. D. Samolyuk, S. I. Golubov, Y. N. Osetsky, and R. E. Stoller, *Philos. Mag. Lett.* **93**, 93 (2013).
- [25] C. Varvenne, F. Bruneval, M. C. Marinica, and E. Clouet, *Phys. Rev. B* **88**, 134102 (2013).
- [26] Q. Peng, W. Ji, J. Lian, X. Chen, H. Huang, F. Gao, and S. De, *Sci. Rep.* **4**, 5735 (2014).
- [27] C. Varvenne, O. MacKain, L. Proville, and E. Clouet, *Acta Mater.* **102**, 56 (2016).
- [28] M. Christensen, W. Wolf, C. M. Freeman, E. Wimmer, R. B. Adamson, L. Hallstadius, P. E. Cantonwine, and E. V. Mader, *J. Nucl. Mater.* **445**, 241 (2014).
- [29] H. Lu, H. Wu, N. Zou, X. Lu, Y. He, and D. Morgan, *Acta Mater.* **154**, 161 (2018).
- [30] S. L. Shang, L. G. Hector, Y. Wang, and Z. K. Liu, *Phys. Rev. B* **83**, 224104 (2011).
- [31] W. W. Xu, S. L. Shang, B. C. Zhou, Y. Wang, L. J. Chen, C. P. Wang, X. J. Liu, and Z. K. Liu, *Phys. Chem. Chem. Phys.* **18**, 16870 (2016).
- [32] V. P. Ramunni and A. M. Rivas, *Mater. Chem. Phys.* **197**, 163 (2017).
- [33] H. B. Huntington and P. B. Ghate, *Phys. Rev. Lett.* **8**, 421 (1962).
- [34] A. Allnatt, I. Belova, and G. Murch, *Philos. Mag.* **94**, 2487 (2014).
- [35] D. Hudson and G. D. Smith, *Scr. Mater.* **61**, 411 (2009).
- [36] G. Sundell, M. Thuvander, and H.-O. André, *Corros. Sci.* **65**, 10 (2012).
- [37] A. Harte, D. Jädernäs, M. Topping, P. Frankel, C. Race, J. Romero, L. Hallstadius, E. Darby, and M. Preuss, *Acta Mater.* **130**, 69 (2017).
- [38] A. Harte, M. Topping, P. Frankel, D. Jädernäs, J. Romero, L. Hallstadius, E. Darby, and M. Preuss, *J. Nucl. Mater.* **487**, 30 (2017).
- [39] G. Sundell, M. Thuvander, P. Tejlund, M. Dahlbäck, L. Hallstadius, and H.-O. André, *J. Nucl. Mater.* **454**, 178 (2014).
- [40] S. N. Balart, N. Varela, and R. H. de Tandler, *J. Nucl. Mater.* **119**, 59 (1983).
- [41] G. M. Hood and R. J. Schultz, *J. Nucl. Mater.* **200**, 141 (1993).
- [42] H. Nakajima, G. M. Hood, and R. J. Schultz, *Philos. Mag. B* **58**, 319 (1988).
- [43] G. M. Hood and R. J. Schultz, *Philos. Mag.* **26**, 329 (1972).
- [44] G. Hood and R. Schultz, *Mater. Sci. Forum* **15–18**, 475 (1987).
- [45] B. P. L. Gruzin, V. S. Emelyanov, G. G. Ryabova, and G. B. Fedorov, in *Proceedings of the Second United Nations International Conference on the Peaceful Uses of Atomic Energy* (United Nations, Geneva, 1958), Vol. 19, p. 187.
- [46] J. Horváth, F. Dymont, and H. Mehrer, *J. Nucl. Mater.* **126**, 206 (1984).
- [47] G. M. Hood, *J. Nucl. Mater.* **139**, 179 (1986).
- [48] M. Lubbehusen, K. Vieregge, G. Hood, H. Mehrer, and C. Herzig, *J. Nucl. Mater.* **182**, 164 (1991).

- [49] G. M. Hood, H. Zou, D. Gupta, and R. J. Schultz, *J. Nucl. Mater.* **223**, 122 (1995).
- [50] G. Neumann and C. Tuijn, *Pergamon Mater. Ser.* **14**, 149 (2008).
- [51] P. A. Burr, M. R. Wenman, B. Gault, M. P. Moody, M. Ivermark, M. J. D. Rushton, M. Preuss, L. Edwards, and R. W. Grimes, *J. Nucl. Mater.* **467**, 320 (2015).
- [52] R. Pasianot and R. Pérez, *J. Nucl. Mater.* **434**, 158 (2013).
- [53] R. C. Pasianot, R. A. Pérez, V. P. Ramunni, and M. Weissmann, *J. Nucl. Mater.* **392**, 100 (2009).
- [54] M. Griffiths, *J. ASTM Int.* **5**, 1 (2008).
- [55] S. I. Choi and J. H. Kim, *Nucl. Eng. Technol.* **45**, 385 (2013).
- [56] T. Seymour, P. Frankel, L. Balogh, T. Ungár, S. Thompson, D. Jädernäs, J. Romero, L. Hallstadius, M. Daymond, G. Ribárik, and M. Preuss, *Acta Mater.* **126**, 102 (2017).
- [57] M. Topping, T. Ungár, C. Race, A. Harte, A. Garner, F. Baxter, S. Dumbill, P. Frankel, and M. Preuss, *Acta Mater.* **145**, 255 (2018).
- [58] D. R. Trinkle, *Philos. Mag.* **96**, 2714 (2016).
- [59] C. C. Battaile, *Comput. Methods Appl. Mech. Eng.* **197**, 3386 (2008).
- [60] A. R. Allnatt and A. B. Lidiard, *Atomic Transport in Solids* (Cambridge University Press, Cambridge, UK, 1993).
- [61] G. H. Vineyard, *J. Phys. Chem. Solids* **3** 121 (1957).
- [62] J. P. Perdew, K. Burke, and M. Ernzerhof, *Phys. Rev. Lett.* **77**, 3865 (1996).
- [63] P. E. Blöchl, *Phys. Rev. B* **50**, 17953 (1994).
- [64] G. Kresse and J. Furthmüller, *Phys. Rev. B* **54**, 11169 (1996).
- [65] M. Methfessel and A. T. Paxton, *Phys. Rev. B* **40**, 3616 (1989).
- [66] H. J. Monkhorst and J. D. Pack, *Phys. Rev. B* **13**, 5188 (1976); L. Vinet and A. Zhedanov, *J. Phys. A: Math. Theor.* **44**, 085201 (2011).
- [67] G. Henkelman, B. P. Uberuaga, and H. Jónsson, *J. Chem. Phys.* **113**, 9901 (2000).
- [68] Y. Zhao, J. Zhang, C. Pantea, J. Qian, L. L. Daemen, P. A. Rigg, R. S. Hixson, G. T. Gray, Y. Yang, L. Wang, Y. Wang, and T. Uchida, *Phys. Rev. B* **71**, 184119 (2005).
- [69] P. Zhang, S. Wang, J. Zhao, C. He, Y. Zhao, and P. Zhang, *J. Appl. Phys.* **113**, 013706 (2013).
- [70] C. Varvenne, O. Mackain, and E. Clouet, *Acta Mater.* **78**, 65 (2014).
- [71] O. Le Bacq, F. Willaime, and A. Pasturel, *Phys. Rev. B* **59**, 8508 (1999).
- [72] T. Angsten, T. Mayeshiba, H. Wu, and D. Morgan, *New J. Phys.* **16**, 015018 (2014).
- [73] G. M. Hood, *J. Nucl. Mater.* **96**, 372 (1981).
- [74] G. M. Hood and R. J. Schultz, *Acta Metall.* **22**, 459 (1974).
- [75] R. Tendler, J. Abriata, and C. Varotto, *J. Nucl. Mater.* **59**, 215 (1976).
- [76] F. C. Frank and D. Turnbull, *Phys. Rev.* **104**, 617 (1956).
- [77] A. C. P. Jain, P. A. Burr, and D. R. Trinkle, Data cite for “Vacancy mediated and interstitial solute transport in Zr from density functional theory calculations”, <http://dx.doi.org/10.18126/M2R04K> (2018).
- [78] JMOL: An open-source browser-based HTML5 viewer and stand-alone Java viewer for chemical structures in 3D (2018), <http://www.jmol.org/>.
- [79] S. J. Clark, M. D. Segall, C. J. Pickard, P. J. Hasnip, M. I. J. Probert, K. Refson, and M. C. Payne, *Z. Kristallogr.* **220**, 567 (2005).
- [80] D. Vanderbilt, *Phys. Rev. B* **41**, 7892 (1990).
- [81] R. H. Byrd, J. Nocedal, and R. B. Schnabel, *Math. Program.* **63**, 129 (1994).
- [82] B. G. Pfrommer, M. Cote, S. G. Louie, and M. L. Cohen, *J. Comput. Phys.* **131**, 233 (1997).
- [83] N. Govind, M. Petersen, G. Fitzgerald, D. King-Smith, and J. Andzelm, *Comput. Mater. Sci.* **28**, 250 (2003).